Taras Shevchenko National University of Kyiv
Faculty of Physics
Department of Nuclear Physics

Optimization of an electromagnetic calorimeter for the LUXE experiment

Mykyta Shchedrolosiev

Translation of thesis submitted to the
Taras Shevchenko National University of Kyiv
in partial fulfillment of the requirement
for MSc degree in Physics
Prepared under supervision of
Prof. Halina Abramowicz, Prof. Aharon Levy,
Prof. Wolfgang Lohmann

Kyiv – 2020

Summary

Shchedrolosiev M.D. "Optimization of electromagnetic calorimeter for the LUXE experiment"
Qualifying work of the master on a speciality 104 — physics and astronomy, specialization "high energy physics". — Taras Shevchenko National University of Kyiv, Faculty of Physics, Department of Nuclear Physics. — Kyiv, 2020.
Research supervisors: Prof. of Tel-Aviv University Halina Abramowicz, Prof. of Tel-Aviv University Halina Abramowicz Aharon Levy
Department research supervisor: Prof. Dr., Aushev V.

Following study is aimed at development and optimization of calorimeter for detection of e^-e^+ pairs in LUXE experiment. This experiment is expected to provide unique data for understanding of physics in strong fields ($> 10^{16}$ V/cm). The energy and position resolution of such calorimeter were calculated for different design of detector using Geant4 simulation, which in the best case are 19.3% and 0.72 mm respectively. Reconstruction method for high flow of the particles is studied, what provide us an opportunity to study interaction of photon with high intensity laser and understand physics in strong fields.

Key words: LUXE, particle physics calorimetry, experimental strong field physics

Анотація

Щедролосьєв М.Д. "Оптимізація електромагнітного калориметра для експерименту LUXE"

Кваліфікаційна робота магістра за спеціальністю 104 —- фізика та астрономія, спеціалізація "фізика високих енергій". — Київський національний університет імені Тараса Шевченка, фізичний факультет, кафедра ядерної фізики. — Київ, 2020.

Наукові керівники: проф. Тель-Авівського університету Halina Abramowicz, проф. Тель-Авівського університету Aharon Levy

Куратор від кафедри: д. ф.-м. н., Аушев В.Є., проф. кафедри ядерної фізики

Дана робота виконана з метою розробки та підготовки експерименту LUXE, який надасть унікальні данні, для вивчення фізики в надвисоких електричних полях ($> 10^{16}$ В/см). Було розроблено симуляцію калориметричної системи для експерименту LUXE на основі Geant4 програмного середовища, досліджено енергетичну та просторову роздільну здатність, при різних конструкційних особливостях детектора, які у найкращих випадках можуть сягати 19.3% та 0.72 мм відповідно. Досліджено метод реконструкції великих потоків частинок, що дозволяє детектувати e^+e^- пари народженні у процесі взаємодії фотонів з інтенсивним лазером, і досліджувати фізику у надвисоких електричних полях.

Ключові слова: LUXE, фізика частинок, калориметрія, експериментальне дослідження фізики у сильних полях

Contents

1   Introduction

The greatest achievement of humanity is overtaking its own imagination. Today one can discover and understand what one is no longer able to imagine. In these days, many remarkable particle physics experiments are aimed to glimpse inside a world that hardly can be conceptualized by human consciousness.

In the last century, one of the most successful quantum field theory - the quantum electrodynamics (QED) provided an outstanding opportunity of precise description of the electromagnetic physics phenomena on microscopic scales. The predictive realization of QED predominantly relies on perturbation theory visualised as Feynman diagrams formalism [9], which provides an unique chance of awareness of the nature on invisible scales using our imagination. Nevertheless, QED is not limited by perturbation theory. In the presence of very strong electric fields $|\boldsymbol{E}| > E_{Schwinger} = 1.32 \times 10^{16}$ V/cm , it predicts that the vacuum itself is expected to become unstable and sparks with spontaneous creation of electron – positron pairs. The corresponding phenomenon is called Schwinger effect [16]. It cannot be described in terms of any finite number of Feynman diagrams. Since, it is related to the nonperturbative regime of quantum physics and can not be illustrative to human's mind.

At the current stage of technological development, it is impossible to achieve a static electrical field of such magnitude. However, using high-power and highly focused lasers enables the production of fields at optical frequencies with root-mean-square (**rms**) values of the electric field close and above the Schwinger field.

This study is aimed at optimising the design of an electromagnetic calorimeter to measure electrons and positrons produced in the interaction of high energy electrons and photons with laser pulses in the LUXE (Laser Und XFEL Experiment) experiment. It is an experiment which is designed to use the high-quality and high-energy electron beam of the European X-Ray Free-Electron Laser Facility (XFEL) and a powerful laser to study the nonperturbative regime of QED. The XFEL is operating with electrons of energies up to $E_e = 17.5$GeV and contains

trains of 2700 electron bunches, each of up to 6×10^9 electrons, that pass at a rate of 10 Hz. For this experiment 5 bunches out of 2700 are taken, what leads to less than 0.2% beam loss. The laser which is expected to be installed for this experiment has a working power range between 30 TW and 300 TW, and a repetition rate of 1 Hz [3].

The scientific goal of LUXE experiment is to study quantum electrodynamics processes in the regime of strong fields. The main physics processes to be investigated are nonlinear Compton scattering and nonlinear Breit-Wheeler pair production. This thesis includes preferably the study of the calorimetric system for reconstruction of laser-assisted one photon pair production (OPPP) assuming the conversion of a high energy photon, overlaping with an intense optical laser beam, into an electron-positron pair.

In the first part of this thesis general properties of the calorimeter design are studied. Basing on the particle occupancy the optimal position and the size of the calorimeter were determined. Spatial and energy resolution are determined for different segmentations and sampling ranges. For this purpose simulations are done in the Geant4 framework [7]. The calorimeter was constructed as a silicon-tungsten sandwich electromagnetic calorimeter following the technology of the LimiCal prototype [?] developed by FCAL collaboration.

In the second part, a reconstruction of the number of particles was done using method which is based on the simple nearest pad neighbour approach. It was shown that for relatively low laser power e.g. 0.2, 0.35, 0.5 Joules, when we have about $\sim 10e^+e^-$ pairs, showers of electrons and positrons which come from the OPPP process can be separated in the calorimeter. For that, the required quality cuts have to be evaluated. However, for the higher laser pulse power 0.7, 0.85 and 1.0 Joules, when most of the showers are aggregated in certain regions of the calorimeter, particles can not be separated. For such cases, the calorimeter is expected to be exploited as a tool for an independent measurements of the number of the e^+e^- particles in the event using the spatial distribution of the deposited energy and comparing it with the prediction due to the deflection in the dipole

field. Such measurement has to be studied in details.

In the third part, the influence of the background on the calorimeter measurement was studied. The background for the standards working regime of the EU XFEL was considered.

In addition to the design and performance estimate of the calorimeter for LUXE, during this master project work on the preparation and testing of LumiCal sensors was performed. In first part the gluing of the silicon sensors to the kapton fan-outs and carbon fiber. In addition supplementary carrying out HV and IV measurements of the pads of the sensor. As the second part, this sensors were installed and operated during the 2019 and 2020 FCAL test-beam at DESY.

2 The LUXE experiment

This section is aimed at description of the LUXE [3] experiment and its scientific objectives. The technical elements of the expected experimental setup are specified in the corresponding chapter.

2.1 Description of the Physics Processes

2.1.1 The Schwinger Effect

As mentioned above, in the last century QED provided outstanding opportunity of the precise description of the physics on microscopic scales based on the perturbation approach. Nonetheless, there are effects that are inaccessible by ordinary perturbation theory. In addition, the prediction of nonpertubative phenomena lacks an experimental verification.

The most popular non-perturbative phenomenon is spontaneous electron-positron pair production (SPP) in a strong static electric field E. This is called the Schwinger effect [16]. The rate of spontaneously created electron-positron pairs in a strong static electric field $\mathbf{E}$ can be written as follows [11]:

$$\frac{\Gamma_{\text{SPP}}}{V} = \frac{m_e^4}{(2\pi)^3} \left(\frac{|\mathbf{E}|}{\text{E}_{\text{c}}} \right)^2 \sum_{n=1}^{\infty} \frac{1}{n^2} \exp\left(-n\pi \frac{\text{E}_{\text{c}}}{|\mathbf{E}|} \right) , \tag{1}$$

where the rate Γ_{SPP} is given per unit volume V, m_e is the electron mass and

$$\text{E}_c \equiv \frac{m_e^2}{e} \simeq 1.3 \times 10^{18} \text{ V/m} , \tag{2}$$

is the so-called Schwinger critical field. It can be noticed that in the corresponding exponential, term $\exp\left(-\pi \frac{m_e^2}{e|\mathbf{E}|} \right)$, the charge e is in denominator and, consequently, it is non-perturbative in $e \propto \sqrt{\alpha}$.

As noted in [11], the this effect have been suggested to play a role in many problems of phenomenological and cosmological interest. However, due to the

technical limitations nowadays, it is impossible to reach a static electric field of such magnitude.

2.1.2   Laser-Assisted One Photon Pair Production

As an alternative to spontaneous pair production in a static electric field one can search for the same effect of boiling vacuum in the so-called laser-assisted one photon pair production (OPPP) - the conversion of a high energy photon in the overlap with an intense optical laser beam into an electron-positron pair. A corresponding process opens an opportunity of obtaining elusive boiling of the QED vacuum and evaluating the Schwinger critical field experimentally.

In the leading order of perturbative theory, the rate of laser-assisted OPPP, Γ_{OPPP}, can be written as follows [10]:

$$\Gamma_{\text{OPPP}} = \frac{\alpha m_e^2}{4\,\omega_{\text{i}}}\, F_\gamma(\xi, \chi_\gamma)\,, \tag{3}$$

where α is the fine structure constant, $k_i = (\omega_{\text{i}}, \mathbf{k_i})$, with $\omega_i^2 = \mathbf{k_i^2}$, is the four-momentum of the initial state photon. $\xi \equiv \frac{e|\mathbf{E}|}{\omega m_e} = \frac{m_e}{\omega}\frac{|\mathbf{E}|}{\text{E}_c}$ is the laser intensity parameter with ω being the laser frequency and $\chi_\gamma \equiv \frac{k \cdot k_i}{m_e^2}\xi = (1 + \cos\theta)\,, \frac{\omega_i}{m_e}\frac{|\mathbf{E}|}{\text{E}_c}$ is the photon recoil parameter. $F_\gamma(\xi, \chi_\gamma)$ is dimensionless factor, it is defined in equation 4. These parameters depend on the electric field $|\mathbf{E}|$ of the laser, the laser frequency ω, and the angle θ between the laser and the photon beam.

According to [11], in the ideal case, when the electromagnetic field of the laser beam can be described as a circularly polarized infinite plane wave, one can write the function $F_\gamma(\xi, \chi_\gamma)$ as a sum over the effective number of laser photons n absorbed by the electron-positron pair [17],

$$F_\gamma(\xi, \chi_\gamma) = \sum_{n>n_{\text{o}}}^{\infty} \int_1^{v_n} \frac{\mathrm{d}v}{v\sqrt{v(v-1)}} \cdot$$
$$\cdot \left[2\,J_n^2(z_v) + \xi^2(2v-1)\left(J_{n+1}^2(z_v) + J_{n\text{-}1}^2(z_v) - 2J_n^2(z_v)\right)\right]\,, \tag{4}$$

with Bessel functions J_n and

$$n_0 \equiv \frac{2\xi\left(1+\xi^2\right)}{\chi_\gamma}, z_v \equiv \frac{4\xi^2\sqrt{1+\xi^2}}{\chi_\gamma}\left[v\left(v_n-v\right)\right]^{1/2}, v_n \equiv \frac{\chi_\gamma\, n}{2\xi(1+\xi^2)}. \tag{5}$$

It is essential to notice that with an increase the laser intensity parameter ξ the number n_0 of swallowed photons for producing e^-e^+ pairs also increases. For large ξ, the function F_γ reaches asymptotic behaviour, and can be represented by a finite value. With condition of $\xi \gtrsim 1/\sqrt{\chi_\gamma} \gg 1$, already for $\xi \gtrsim 1$ and $\chi_\gamma \lesssim 1$ F_γ can be represented [15]:

$$F_\gamma(\xi,\chi_\gamma) = \frac{3}{4}\sqrt{\frac{3}{2}}\,\chi_\gamma\, \mathrm{e}^{\left[-\frac{8}{3\chi_\gamma}\left(1-\frac{1}{15}\xi^{-2}+\mathcal{O}(\xi^{-4})\right)\right]}, \tag{6}$$

The corresponding form of the equesion is given with a precision at $\mathcal{O}(\xi^{-4})$. It is clear that the asymptotic form of $F_\gamma(\xi,\chi_\gamma)$ is not pertrubative in the electromagnetic coupling. The asymptotic form of the rate for laser-assisted OPPP reads:

$$\Gamma_{\mathrm{OPPP}} \to \frac{3}{16}\sqrt{\frac{3}{2}}\,\alpha\, m_e\left(1+\cos\theta\right)\frac{|\mathbf{E}|}{\mathrm{E}_c}\exp\left[-\frac{8}{3}\frac{1}{1+\cos\theta}\frac{m_e}{\omega_i}\frac{\mathrm{E}_c}{|\mathbf{E}|}\right]. \tag{7}$$

In such a form the rate is reciprocal to the Schwinger pair production rate in a static electric field. Corresponding conformity between laser-assisted OPPP and SPP in a static electric field occurs for a large laser intensity parameter $\xi \gg 1$ which corresponds to a quasi-static electric field of the laser. Also, during laser-assisted OPPP, there is an electric field is enhanced by the relativistic boost factor ω_i/m_e, in the rest frame of the produced electron-positron pair. As a result, there is a field of the order the Schwinger critical value E_c. Consequently, laser-assisted OPPP is a good alternative to determine the Schwinger critical field experimentally from the measurement of its rate of e^+e^- pairs production at $\xi \gtrsim 1/\sqrt{\chi_\gamma} \gg 1$.

2.1.3   Utilizing Bremsstrahlung Photons for OPPP Study

Currently, there are no photon beam experiments of the required quality and energy that could be used for the purpose of studying laser-assisted OPPP. However, there are high-energy electron beam facilities that could be used for this purpose. By using a target to convert electrons into a high energy photon beam, which can then be intersected with a high-intensity laser beam. For instance, the electron beam of the European XFEL [1] facility in Hamburg can be suited for such purposes.

   The nature of a Bremsstrahlung spectrum has been already well studied [14]. When the target thickness is much smaller than the radiation length of its material $X \ll X_0$, the Bremsstrahlung spectrum can be written as follows:

$$\omega_i \frac{\mathrm{d}N_\gamma}{\mathrm{d}\omega_i} \approx \left[\frac{4}{3} - \frac{4}{3}\left(\frac{\omega_i}{E_e}\right) + \left(\frac{\omega_i}{E_e}\right)^2 \right] \frac{X}{X_0}, \tag{8}$$

where $\mathrm{d}N_\gamma/\mathrm{d}\omega_i$ is the spectrum of the photons generated by an electron of energy E_e impinging on the target.

   Having the spectrum $\mathrm{d}N_\gamma/\mathrm{d}\omega_i$ of flickering photons generated by Bremsstrahlung, the rate of laser-assisted BPPP, Γ_{BPPP}, with corresponding photons can be found by integrating the spectrum.

$$\begin{aligned}
\Gamma_{\mathrm{BPPP}} &= \frac{\alpha\, m_e^2}{4} \int_0^{E_e} \frac{\mathrm{d}\omega_i}{\omega_\mathrm{i}} \frac{\mathrm{d}N_\gamma}{\mathrm{d}\omega_i}\, F_\gamma(\xi, \chi_\gamma(\omega_i)) \\
&= \frac{\alpha\, m_e^2}{4} \frac{\chi_e}{E_e} \int_0^{\chi_e} \frac{\mathrm{d}\chi_\gamma}{\chi_\gamma} \frac{\mathrm{d}N_\gamma}{\mathrm{d}\chi_\gamma}\, F_\gamma(\xi, \chi_\gamma),
\end{aligned} \tag{9}$$

where $\chi_e \equiv k \cdot k_e\, \xi/m_e^2 = (1 + \cos\theta)\omega E_e \xi/m_e^2$ is the electron recoil parameter.

   At high laser intensities, $\xi \gtrsim 1/\sqrt{\chi_e} \gg 1$, the laser-assisted BPPP rate can be expressed as following:

$$\Gamma_{\mathrm{BPPP}} \to \frac{\alpha\, m_e^2}{E_e} \frac{9}{128} \sqrt{\frac{3}{2}}\, \chi_e^2\, e^{-\frac{8}{3\chi_e}\left(1 - \frac{1}{15\xi^2}\right)} \frac{X}{X_0}. \tag{10}$$

Finally, for high laser intensity, asymptotic behaviour can be reached. In that case the Schwinger critical field - E_c can be extracted by measuring the rate of such laser-assisted BPPP, which for high ξ has the following form:

$$\Gamma_{\mathrm{BPPP}} \to \frac{9}{128}\sqrt{\frac{3}{2}}\,\alpha\,E_e\,(1+\cos\theta)^2 \left(\frac{|\mathbf{E}|}{\mathrm{E}_c}\right)^2 \exp\left[-\frac{8}{3}\frac{1}{1+\cos\theta}\frac{m_e}{E_e}\frac{\mathrm{E}_c}{|\mathbf{E}|}\right]\frac{X}{X_0}. \quad (11)$$
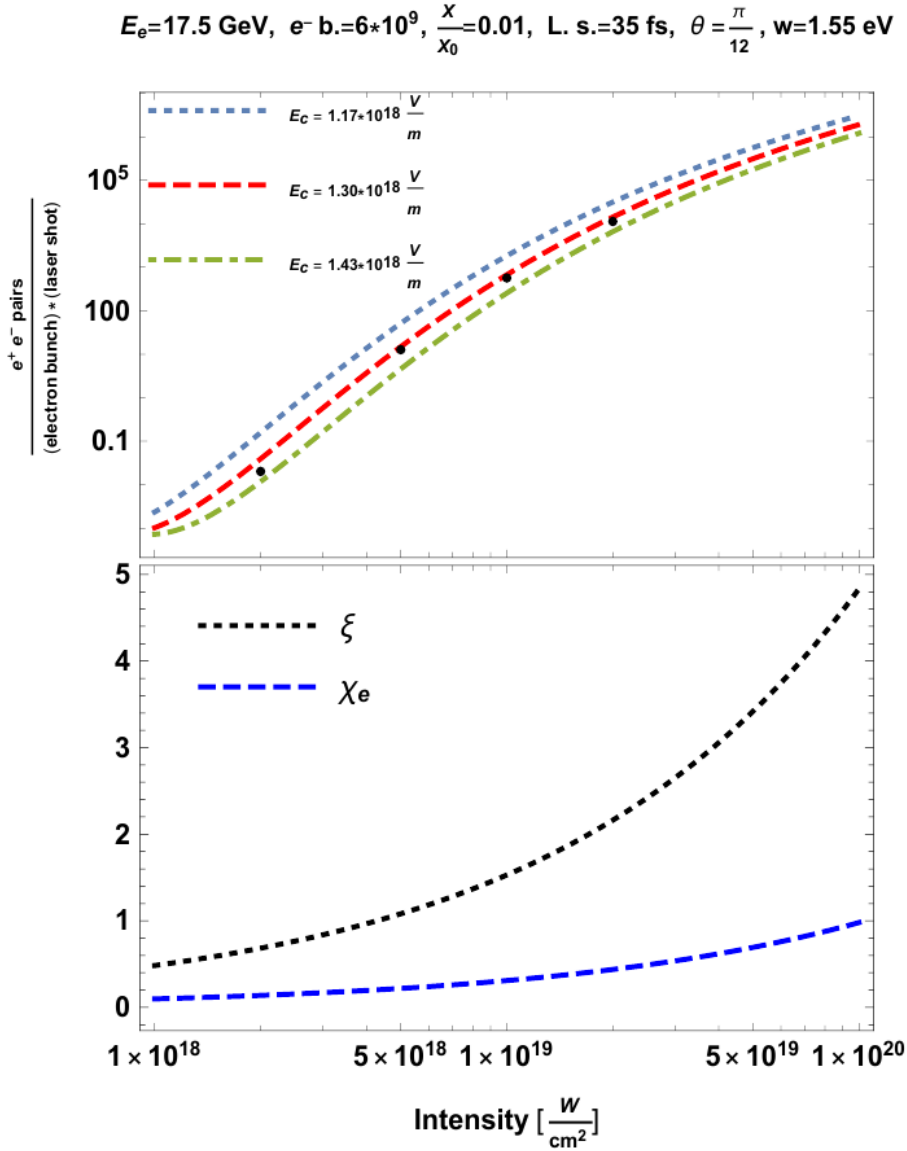
Figure 1: Simulation results from [11]. Number of $e^\pm$ pairs produced per electron bunchs is shown.

The simulation of laser-assisted BPPP for different laser-intensity [11] is shown in figure 1. Total number of $e^{\pm}$ pairs produced per electron bunch as a function of the laser intensity is built (number of electrons - $6 \cdot 10^9$, energy of electrons - $7.5 GeV$, target thickness - $X/X0 = 0.01$, laser shot duration - 35 fs, laser frequency - $1.55 eV$, laser wavelength - 800 nm, crossing angle - $\pi/12$). The dotted line shows the same analytic prediction where the Schwinger critical field deviates by a factor of k = 0.9 (k = 1.1) from nominal value. On the bottom panel of the figure 1, the laser intensity parameter and the electron recoil parameter are shown. It demonstrates how measuring the number of the $e^{\pm}$ pairs for the different intensity of the laser one can determine the Schwinger critical field.

In the next parts, the experimental setup and the mechanism of detecting $e^- e^+$ pairs are described in details.

2.2   Practical Implementation of the Experiment

As was said above, the EU-XFEL facility gives us an opportunity of obtaining high-quality and high-energy electrons. Following experimental facility is appropriate for studying Bremsstrahlung photon pair production and determining the Schwinger critical field.

2.2.1   Experimental Setup

The European XFEL can run with the electron energies up to 17.5 GeV and the beam contain trains of 2700 electron bunches, each one of up to 6×10^9 electrons, at a rate of 10 Hz. For extracting the particles from the XFEL beam line a spatial extraction kicker is used. Due to the limitation of the response time it is only possible to extract up to five bunches out of 2700 for the LUXE experiment.

The EU-XFEL tannels and buildings are shown in figure 2. The electron extraction point will be at the end of the LINAC before the XTD2 and XTD1 tunnels. The experimental setup is planned to be installed at the currently unused annex of the XS1 shaft.
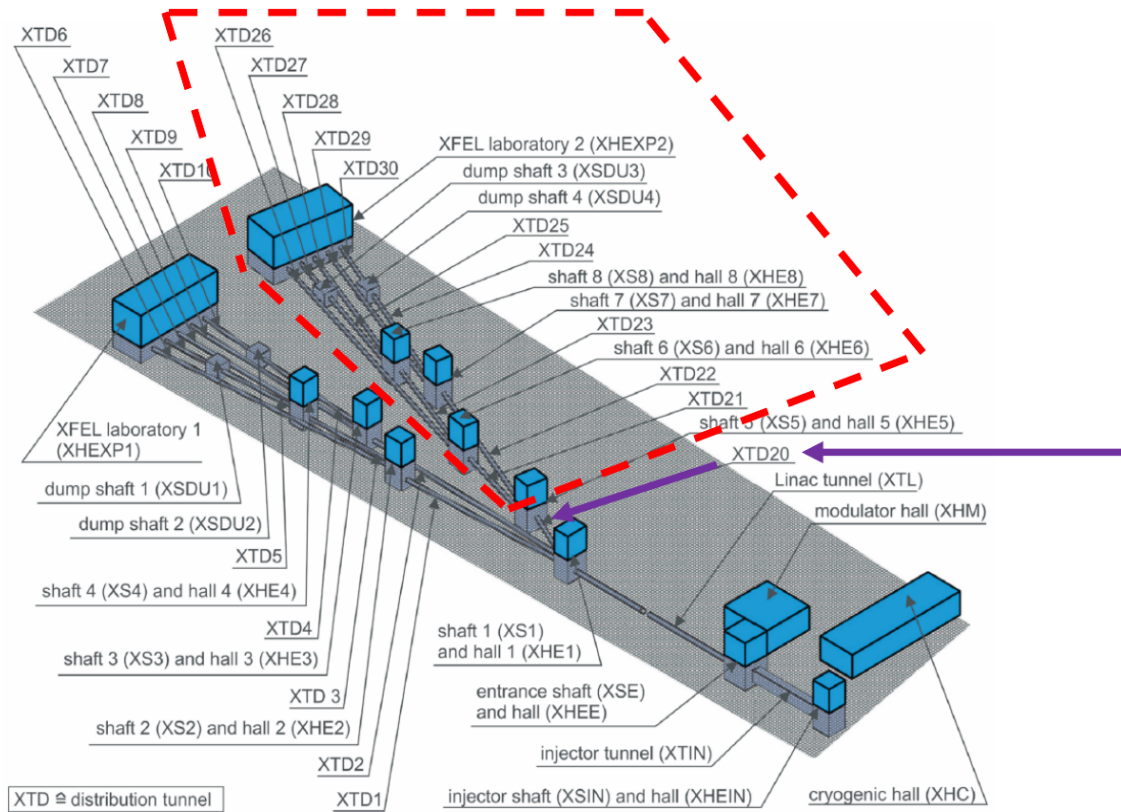
Figure 2: Illustration of European XFEL tunnels and buildings. Red dashed line shows areas that was not yet constructed. The purple arrows point to the XS1 shaft where the LUXE experiment is expected to be installed. (Picture is taken from [3])

The basic idea of the LUXE experiment is collision of two types (figure 3). The first one is to study colliding electrons with a high-power, tightly focused laser beam directly ($e^- + n\gamma_L \rightarrow e^-\gamma$). The second one is first converting electrons to photons by Bremsstrahlung and then collide them with the laser beam photons ($\gamma + n\gamma_L \rightarrow e^+e^-$). The latter is the main object of study of this diploma.

Two different setups are needed. In the first version no target is installed and electrons are directly taken from the deflection system, which includes the kicker and 4 septa magnets which direct the selected bunch of electrons into the XS1 annex. Then, after passing the shielding these electrons immediately collide with a high intensity laser beam, as shown in the upper part of figure 4. After that,
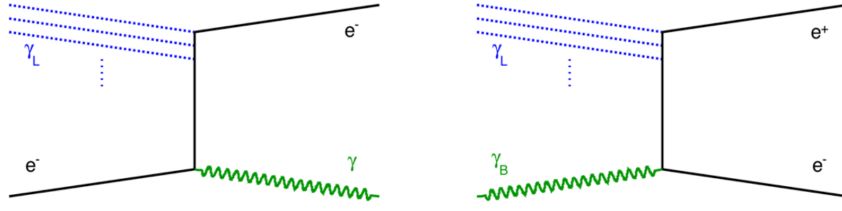
Figure 3: Illustration of $e^- + n\gamma_L \to e^-\gamma$ and $\gamma + n\gamma_L \to e^+e^-$ processes.

both electrons and positrons are deflected by the magnetic field and guided into the detector system. This system measures the number of electron-positron pairs that were produced in the non-linear Compton process. Residual and scattered photons continue their movement to the gamma-ray spectrometer system which evaluates the final luminosity of the beam.

In the second version of setup (bottom part of figure 4) the electrons first are converted to photons by Bremsstrahlung, using a 35 microns tungsten foil. Subsequently, a system of collimators is installed to form the beam and to clean the background before the initial detector system, that measure the number of photons in the beam by determining the number of $e^\pm$ pairs after the tungsten target. A beam dump is added for the electrons which pass the target without conversion to the Bremsstrahlung photons. The pair detection system is different because for the $\gamma + n\gamma_L \to e^+e^-$ process the maximum number of electron-positron pairs that will be produces is $\sim 40 - 50$ pairs and Cerenkov counter is not required anymore. Instead, for a precise measurement of the electron and positron energies. The Cerenkov counter is replaced by tracker system but calorimeter system remains the same. In both setups, a shielding is required before the laser-beam interaction point (IP).

One of the requirements on the high power laser is that its intensity parameter has to significantly exceed 1. The parameter can be defined as following:

$$\xi = 2.370 \left(\frac{I}{10^{19}\,\text{W/cm}^2} \right)^{1/2} \left(\frac{1\,\text{eV}}{\omega} \right) \tag{12}$$

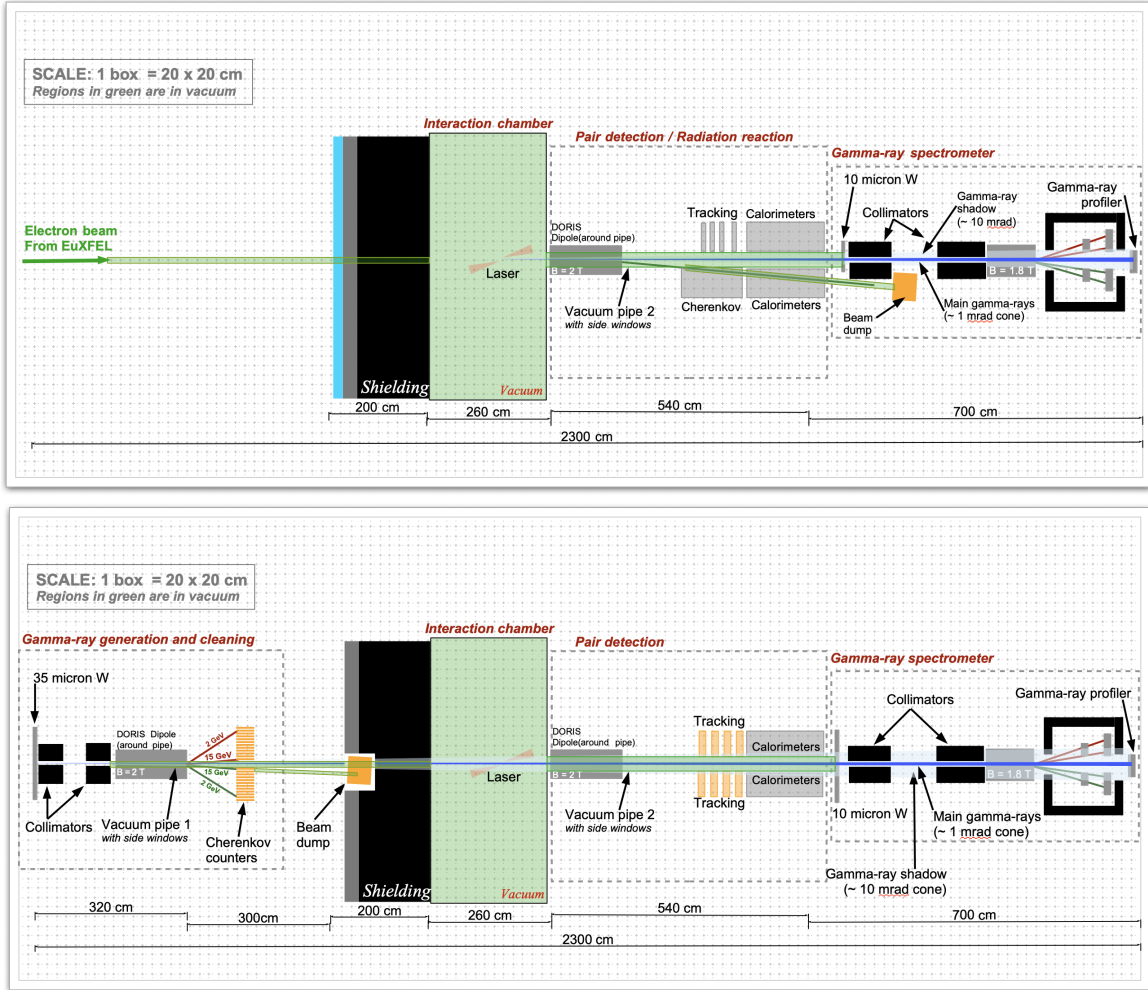The laser which is expected to be adopted for this experiment has a nominal power

Figure 4: Draught of the experimental setup for the $e^- + n\gamma_L \rightarrow e^-\gamma$ (top) and $\gamma + n\gamma_L \rightarrow e^+e^-$ (bottom) processes. The e^- beam comes from the left (Picture is taken from [3])

ranging from 30TW to 300TW with a repetition rate of 1 Hz. The duration of the pulse which is expected to be used is 30 fs. The energy per pulse varies from 1 to 9 J. The losses in the optics and transport for $(8 \times 8)W/cm^2$ focal spot are $1.6 \cdot 10^{19}W/cm^2$ and $1.6 \cdot 10^{20}W/cm^2$ FWHM respectively. Minimizing the laser focus to $(3 \times 3)\mu m^2$ would maximize the intensities up to $1.1 \cdot 10^{21}W/cm^2$. The laser system is supposed to be as small as possible to require less physical space and is easier to accommodate with the existing infrastructure.

2.2.2   Particle Rate

The number of electron-positron pairs that are foreseen to be produced in the laser interaction point was shown on figure 1. The full list of expected particles in different regions of the setup is shown in the following table.

Location	particle type	rate for $\xi = 6.5$	rate for $\xi = 1.2$
e^- detector behind converter	e^-, $E_e < 13$ GeV	2×10^7	
e^+ detector behind converter	e^+	9×10^4	
photons after converter	γ	1.3×10^8	
$e^\pm$ detector behind IP	e^-/e^+	350	1×10^{-2}
Photon detector	γ	1.3×10^8	
Photon detector	e^+ and e^-	160	

Table 1: Number of the particles for the $\gamma + n\gamma_L \rightarrow e^+e^-$ setup, $E_{beam} = 17.5$ GeV and $1.5 \cdot 10^9$ electrons per bunch.

2.2.3   Detector Regions and e^-e^+ pair detector system

The detector system after the IP for the electron-positron pairs that were produced in the BPPP process aims at counting the number of particles and measuring their energies. A silicon pixel tracker followed by a calorimeter will be installed for this purposes. Such a system can serve for relatively small particle rates up to 110 positrons and electrons. In addition to the main goals this system could help with suppression of the background. In principle, calorimeter and tracker could be used as an independent measurement of the number of particles and their energy, thereupon they can be exploited for the cross calibration of each other.

In case of electron-positron pairs after Bremsstrahlung, the tungsten converter has to be measured for providing the value of the photon flux. The number of particles after the tungsten foil reach $\sim 10^6$; The Cherenkov counter is the most common solution for detecting such a big flow of particles. The whole system is likely to be triggered either by the laser pulse or by the beam crossing the IP. The maximum rate expected for corresponding system is 10 Hz.
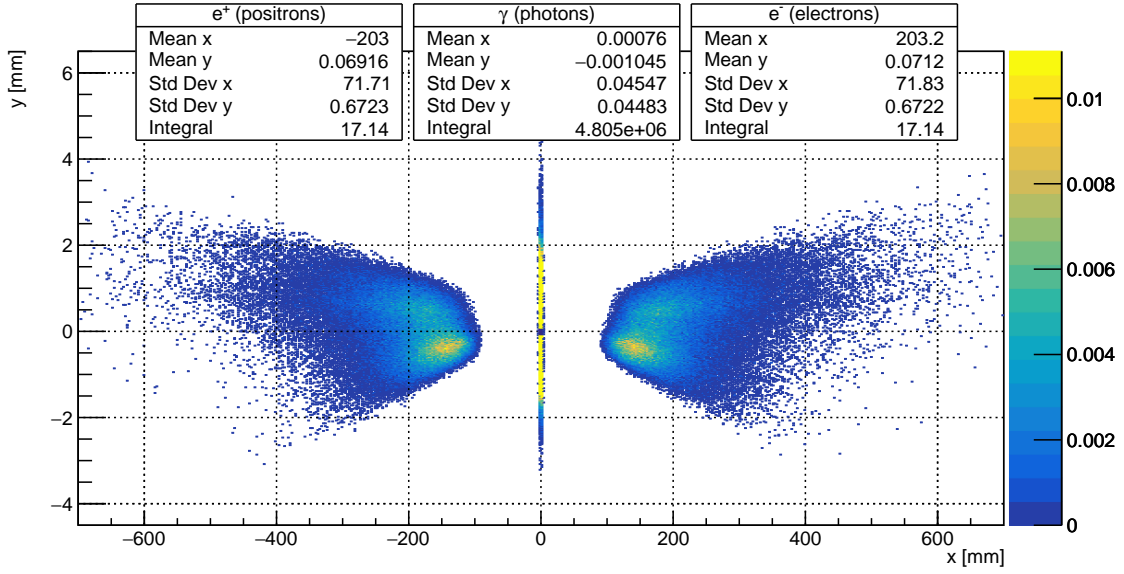
Figure 5: Occupancy of $e^{\pm}$ for $\gamma + n\gamma_L \rightarrow e^+e^-$ as function of the transverse and vertical coordinates after passing 1.4 T magnet.The occupancy is calculated for $E_e = 17.5$ GeV and $\xi=2.5$ on the 5m distance from IP. Distribution is averaged by 1000 bunch crossings

The e^+e^- pairs after the interaction point and magnet deflection have the shape of so-called butterfly. It can be seen on figure 5 that one arm of the distribution covers the region of $\sim$5mm in y-axis and $\sim$550mm in x-axis. In order to cover this region of e^- and e^+ particles and to avoid photons in the middle two arms of calorimeter are needed.

The calorimeter used for this measurement will have a shape of thin and long rail in order to detect highly scattered particles in the transverse plane. More details about the calorimeter for detection of electron-positrons pairs are described in next part.

3 Electromagnetic Calorimeter for $e^{\pm}$ Reconstruction

The electromagnetic calorimeter will be the part of $e^{\pm}$ pairs detection system. It will be placed after the tracker, providing an additional measurement to improve e^+e^- spectra reconstruction, as well as procuring a tool for rejection of low energy background. It also can serve as an independent apparatus for estimating the number of particles which were created at IP. Calorimeter with small transverse shower profile size is required for such purposes. LumiCal and BeamCal are ultracompact calorimeters that are to be install at very forward region of future International Linear Collider (ILC) and Compact Linear Collider (CLIC) experiments were developed for similar purposes [2]. Thus, it was decided to use the design similar to the ultracompact LumiCal calorimeter.

The existing prototype of the LumiCal is a sampling calorimeter composed of 20 layers of 3.5 mm (one radiation length) thick tungsten plates as an absorbers and silicon sensors placed between tungsten plates. However, in case of the LumiCal cylindrically symmetrical design of the detectors is used. In case of the LUXE experiment there is no need in sensors of such form and it was decided to use rectangular geometry to cover the regions occupied by electrons and positrons shown on the figure 5. The length of the calorimeter is 5mm in y-axis and 550mm in x-axis. The overall thickness of 20 tungsten and sensor planes is about 10-15cm. The calorimeter will be installed on the 5 m distance from the IP.

One detecting plate of the sensor shown on figure 6 consists of 320 μm thick high resistivity n-type silicon wafer, where some percent of the remaining charge in shower is collected in order to later evaluate the energy of the reconstructed particle. The bias voltage is supplied to the n-side of the sensor by a μm flexible Kapton–copper foil, glued to the sensor with a conductive glue. Front side of the sensor glued to the 120 μm thick flexible Kapton foil. Contacts of the front Kapton fan-out is bounded to the p-type silicon pads using ultrasonic wire bonding. All the layer is installed on carbon support structure.
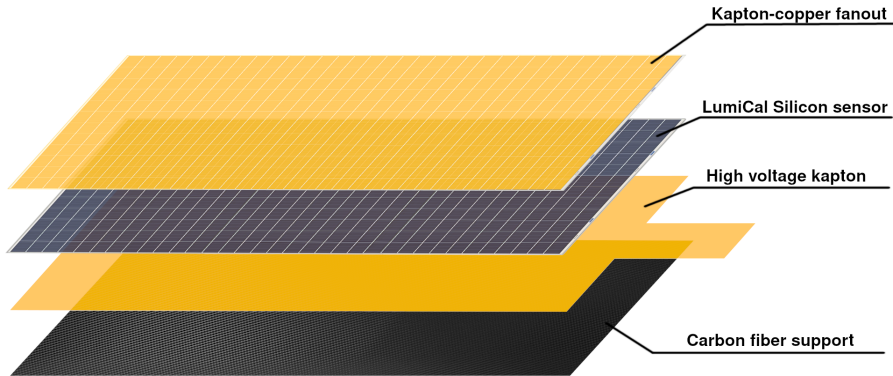
Figure 6: Visualization of detector plate components. The thickness of adhesive layers between components is about 10-15 μm. The overall thickness is about 650 μm

3.1 Simulation of LUXE ECAL in Geant4

The Geant4 framework [7] is used for the simulation of the detector. Different designs were tested. On the initial stage of this analysis it was tried to use sensors of the form of existing LumiCal prototype [4]. However, it was decided to leave a simple rectangular design because of technical reasons.

The list of the sensor parameters that were used for simulation:

- Air gap between layers of the sensor: 0.2 mm

- Silicon sensor: 0.32 mm

- Carbon support: 0.1 mm

- Aluminium conductive glue: 0.02 mm

- Tungsten absorber: 3.5 mm

- Density of the absorber: 19.3 g/cm^3

- Front fan-out with epoxy glue: 0.15 mm

- Back fan-out with epoxy glue: 0.15 mm
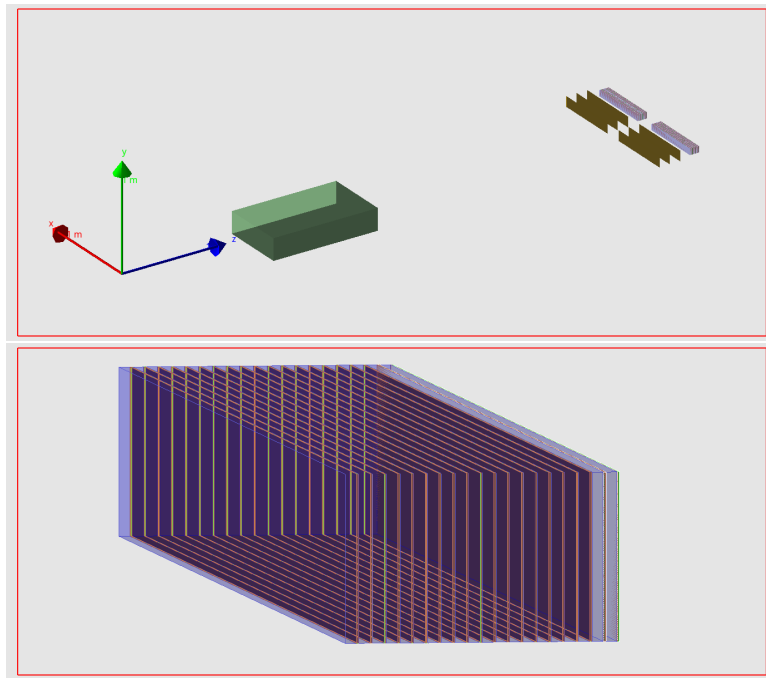
Figure 7: Upper plot: illustration of magnet and two arms of the calorimeter in Geant4 simulation (plates of the tracker is shown for illustration only), IP is placed in the beginning of the coordinates; Lower plot: illustration of one arm of the calorimeter.

3.2   Clustering and Reconstruction Algorithm

When a particle hits the volume of the calorimeter it creates so-called hits in the cells of the silicon. The charge that was collected in a cell than can be matched to equivalent energy. Having the energy absorbed in every cell, it is still an issue of calculations, how to produce high level physical quantities such as particle energy and position from low level information about hits energy and position.

Clustering algorithm followed by particle parameters reconstruction is used for such purpose. In our case nearest neighbour algorithm was used, the procedure can be divided into the following steps:

1. Joining all the cells into towers

2. Choosing seed towers

3. Collecting all the hits into clusters

4. Merging clusters

5. Reconstructing energy and position

Here following steps are described in details:

Step 1: Tower is a structure that consist of cells that were summed up in longitudinal direction with the same transverse position. After we collect all the hits energies in towers we have two dimensional distribution of energy absorbed in towers. Example of such distribution is demonstrated on figure 8.
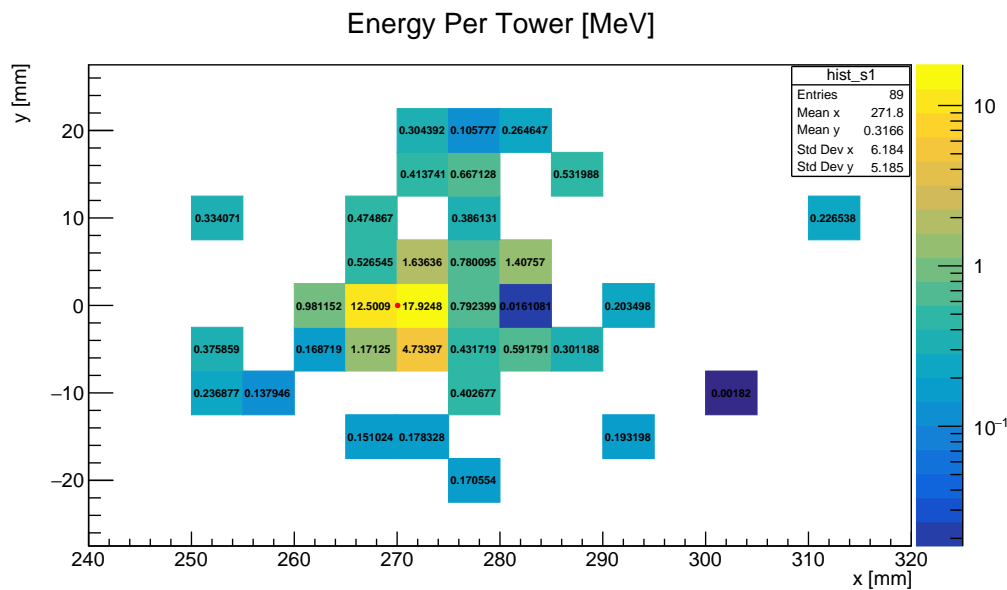

Figure 8: Distribution of energy absorbed in towers. Red point is position of the particle that hits the calorimeter. One rectangle on the plot demonstrate the tower size in transverse plane. Every tower has the longitudinal depth of 20 layers. Number above the rectangle is energy absorbed in tower (given in MeV).

Step 2: During this step all the local maximums that have more than one active pad inside the tower is determined as seeds. Seed is the tower around which we will collect other hits to form the cluster.

Step 3: All the towers should be connected to seeds to form the clusters on this step. For this, we firstly anchor every seed to individual cluster, then we iterate over all the pads and connect every pad to the closest (within 1 pad distance in x or y direction) neighbour of the highest energy and that was already

connected to some cluster. We than repeat the procedure until all the hits are collected into clusters.

Step 4: On the figure 8 it can be seen that there are a lot of local maximums that are outlying from the global maximum and do not really correspond to any particle. On this step the goal is to connect such small energetic island to the cluster that we expect to correspond to a particle. For this purpose we iterate over all the clusters and merge one cluster with another nearest to it if it satisfies the following criteria: 1) $NearestTrackDistance \geq 16mm$ - Using virtual plates in simulation we detect all the tracks and its momentum directions. The condition is that if there is no track within 16mm from cluster this cluster should be merged. In other words if there is no track that can be associated with this cluster, it should be merged (another option, when one wants to do reconstruction independently from tracker one should use cut on the distance, that should be bigger than Moliery Radius instead $distance(cluster_1, cluster_2) \geq 8mm$; 2) The second criteria is that the energy of a cluster should be bigger than 20 MeV - $E_{cluster} \leq 20MeV$.

Step 5: It should be noted that this step is done together with step 4, because merging clusters requires estimate of the position of the cluster. It is done by averaging over all the hits of the cluster, using the hit cell center, (x_i, y_i, z_i), and a weight function, w_i. Position of the cluster (shower center) and its energy is calculated as following:

$$\bar{x}_{cluster} = \frac{\sum_i x_i w_i}{\sum_i w_i} \ , \quad E_{cluster} = \sum_i E_i \ , \tag{13}$$

in the same way $\bar{y}_{cluster}$ and $\bar{z}_{cluster}$ are calculated. E_i is the energy of individual hit cell, w_i can be chosen in two ways: weighting by the hit energy $w_i = E_i$ or in more advanced approach with the logarithmic weighting [5]:

$$w_i = max\{ \ 0 \ , C_0 + \frac{E_i}{E_{cluster}} \} \ . \tag{14}$$

where C_0 is a constant that performs as an threshold on energy of the hit. As a

result only hits that have a higher contribution to the cluster energy are taken into account when calculating cluster position. The numerical values of C_0 are determined empirically for every granularity of ECAL calorimeter. Exact values will be studied in the following sections.

3.3 Calibration Procedure

The main purpose of calorimeters is to measure the energy of particles. The main principle that gives an opportunity of measuring the energy with electromagnetic calorimeter is that the energy released in the detector material by the charged particles of the shower, mainly through ionization and excitation, is proportional to the energy of the incident particle [8].

The integral length of the shower T_0, can be found as the sum of all ionization tracks due to all charge particles in cascade, is proportional to the number of particles in the shower. $T_0 \sim X_0 \frac{E_0}{E_c}$, where E_0 is original particle energy, E_c is defined as the energy at which the rate of energy loss per radiation length equals the total energy of the particle. Also, $\frac{E_0}{E_c}$ can be interpret as the number of particles in the shower. In this way, from measuring of the signal produced by the charged tracks of the cascade initial particle energy E_0 can be found.

First of all, calibration procedure of simulated calorimeter has to be performed. Every particle create a shower inside the calorimeter, some percent of the general shower energy is absorbed in silicon layer and this among of energy can be measured. A sampling calorimeter is characterized with so-called sampling fraction $f_{sample} = E_{visible}/E_{total\ absorbed}$. Corresponding fraction is to be defined during.

For this, we generate 10000 Monte Carlo events for every energy from 4 GeV to 11 GeV. Then distribution of energy absorbed in silicon layers for a fixed energy of the particle can be obtained for different energies as shown on figure 9. Every peak within region of 1.5 **rms** is fitted with the Gaussian function and standard deviation with mean values of Gaussian is calculated.

It was checked that with 20 layers of absorbed leakage energy in such calorimeter is negligible. Such-wise, we can assume that all energy of the particle is
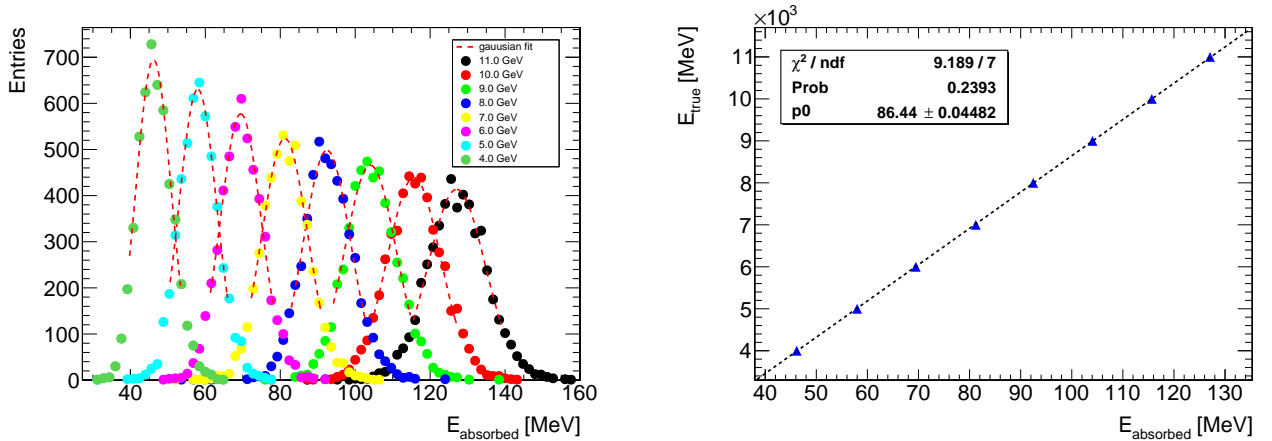
(a) Absorbed energy distribution for the particles with energies in the range from 4 to 11 GeV. Every distribution corresponds to 10000 Monte Carlo events. Peaks are fitted with the Gaussian distribution within 1.5 **rms** from mean value. Gaussian function is integrated within bin ranges.

(b) Evaluating sampling fraction as a parameter of linear function $p0$. On the vertical axis there is the energy of the particle that collides in the calorimeter volume E_{true}, on the horizontal axis energy absorbed in the silicon layers is shown $E_{absorbed}$.

Figure 9: Calibration procedure based on Monte Carlo data.

absorbed in the volume of calorimeter. After obtaining mean and standard deviation of the absorbed energy for each energy one can evaluate sampling fraction as shown on right plot in figure 9.

3.4   Energy Resolution

The ideal calorimeter is the one with infinite size and no response deterioration due to instrumental effects. The intrinsic energy resolution of such calorimeter is mainly due to fluctuation of the track length T_0. Track length is proportional to the number of track segments in the shower. The shower development is stochastic process, and intrinsic energy resolution can be calculated from purely statistical arguments [8]:

$$\sigma(E) \sim \sqrt{T_0}\,, \tag{15}$$

what explains 'stochastic term' in full formula for energy resolution.

The actual energy resolution of a realistic calorimeter can be written as in the formula 16:

$$\frac{\sigma(E)}{E} = \frac{a}{\sqrt{E}} \oplus \frac{b}{E} \oplus c \,. \tag{16}$$

where the symbol $\oplus$ means a quadratic sum. The terms of this formula can be interpreted in the following way:

- a - term called "stochastic term" its nature lies in intrinsic fluctuation as described above. In sampling calorimeters the energy deposited in the active medium fluctuates event by event because the active layers are interleaved with absorber layers. These fluctuations, which are called "sampling fluctuations" and represent the most important limitation to the energy resolution of these detectors, are due to variations in the number of charged particles which cross the active layers.

- b - term corresponds to error that comes from the electronic noise of the readout chain and depends on the detector technique and on the features of the readout circuit. In the simulation we do not simulate readout system, so, this term can be ignored.

- c - term corresponds to instrumental effects that cause variation of the calorimeter responds for different impact points and give rise to response nonuniformities.

In the LUXE experiment energy resolution of the calorimeter is very important because it is important to measure the spectrum of the particles. Energy resolution was calculated for different numbers of silicon sensor plates in the calorimeter. Starting from the first layer and from the last we removed one plate from the front and one from the back in each installation variation. Idea is to leave the silicon plates in the center which absorb majority of the energy comparing to the other sensors. In this calorimeter it is layers number 8-9.

The Monte Carlo was generated for 6 different setups with number of layers in range from 20 to 10. For each 11 different energies were used in range from 4
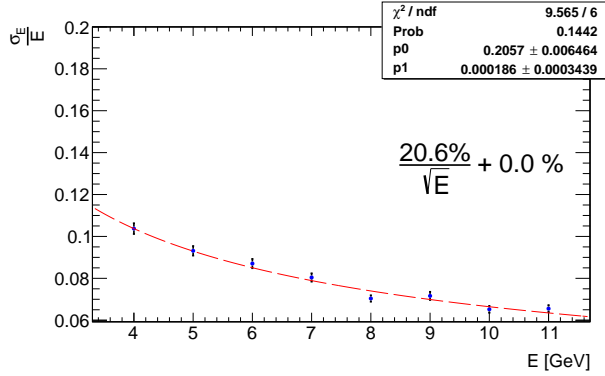
to 11 GeV with the 10000 events per each data set. The corresponding results are shown on figure 10.
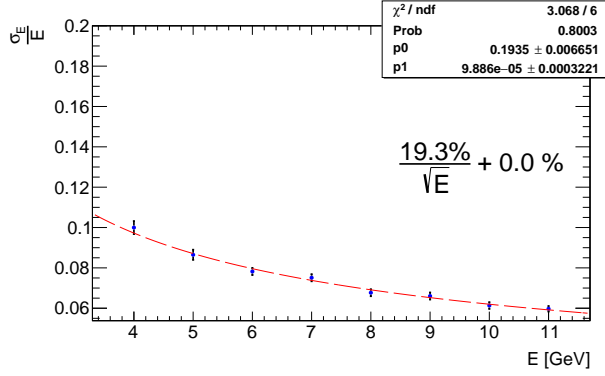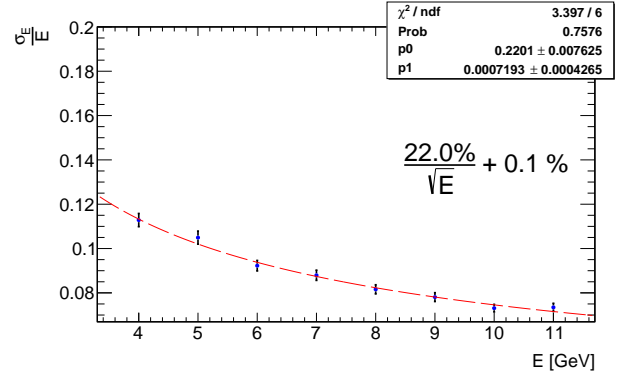

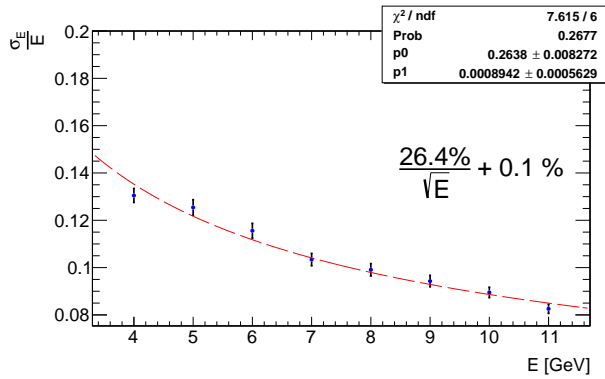(a) 20 layers of silicon
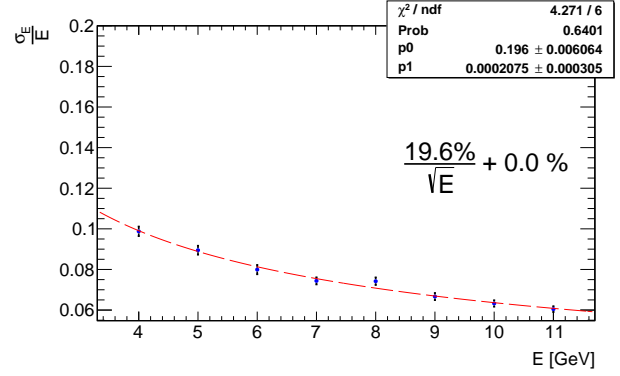
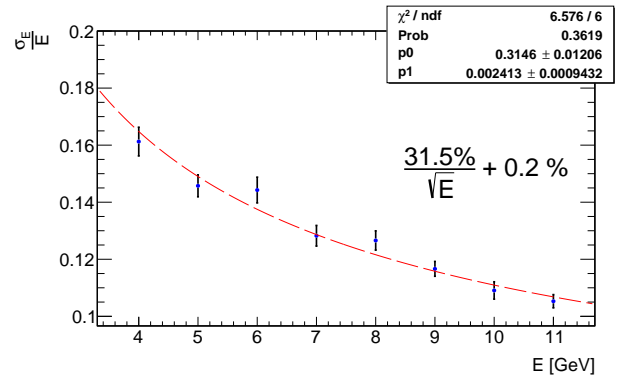(b) 18 layers of silicon

(c) 16 layers of silicon

(d) 14 layers of silicon

(e) 12 layers of silicon

(f) 10 layers of silicon

Figure 10: Energy resolution for different number of the detector silicon plates. Data generated for energies in range from 4 to 11 GeV. Each distribution is fitted with $\frac{\sigma(E)}{E} = \frac{a}{\sqrt{E}} \oplus c$ function. $p0$ corresponds to a-term and $p1$ to c-term.

3.5   Positional Resolution

In addition to calculating the energy of the particle, it is equally important to measure the coordinate of the particle entering the calorimeter. Usually, this calculation is performed by averaging the central coordinate of the cluster by the coordinates of the hits. As mentioned before, the coordinates of the particle that formed the drain are used for the procedure of merging clusters. In the LUXE experiment, information about the coordinate of a particle is also an additional measurement of its energy, using a magnet and matching the coordinate to the energy of the particle (this procedure will be described in more detail in the following sections).

Similar to calorimeter depreciation by reducing the number of plates, the calorimeter also becomes cheaper and easier to manufacture with reduced calorimeter granularity. The minimum cell size considered in this study is 5×5 mm. Under this condition, 11 Y-axis pads and 110 X-axis pads are placed on one silicon sensor plate. The number of cells was further reduced to a minimum of 3 Y-axis cells and 30 X-axis cells.

In our calculations, by positional resolution we mean the standard deviation σ of the distribution of the differences between the center of the cluster on the X or Y axis and the corresponding true particle coordinate, which is fixed in the tracker $\sigma[x - x_{tr}]$.

As shown in many previous studies, for example [13], positional resolution is also a function of particle energy. But, firstly, for large energies, such as we have for OPPP spectrum (4-11 GeV), the resolution changes very weakly, and secondly, we aim to calculate the resolution for the particle of energies that we have in our experiment (~ 6 GeV).

To calculate the coordinate resolution, the monoenergetic Monte Carlo of the energy 6 GeV was taken. The particles were launched strictly perpendicular to the plane of the detector. The initial coordinate of generated particle was blurred within a single pixel, using the Geant4 function `G4RandFlat:: shoot(y_min, y_max)`. The simulation results for different calorimeter pad sizes are shown on
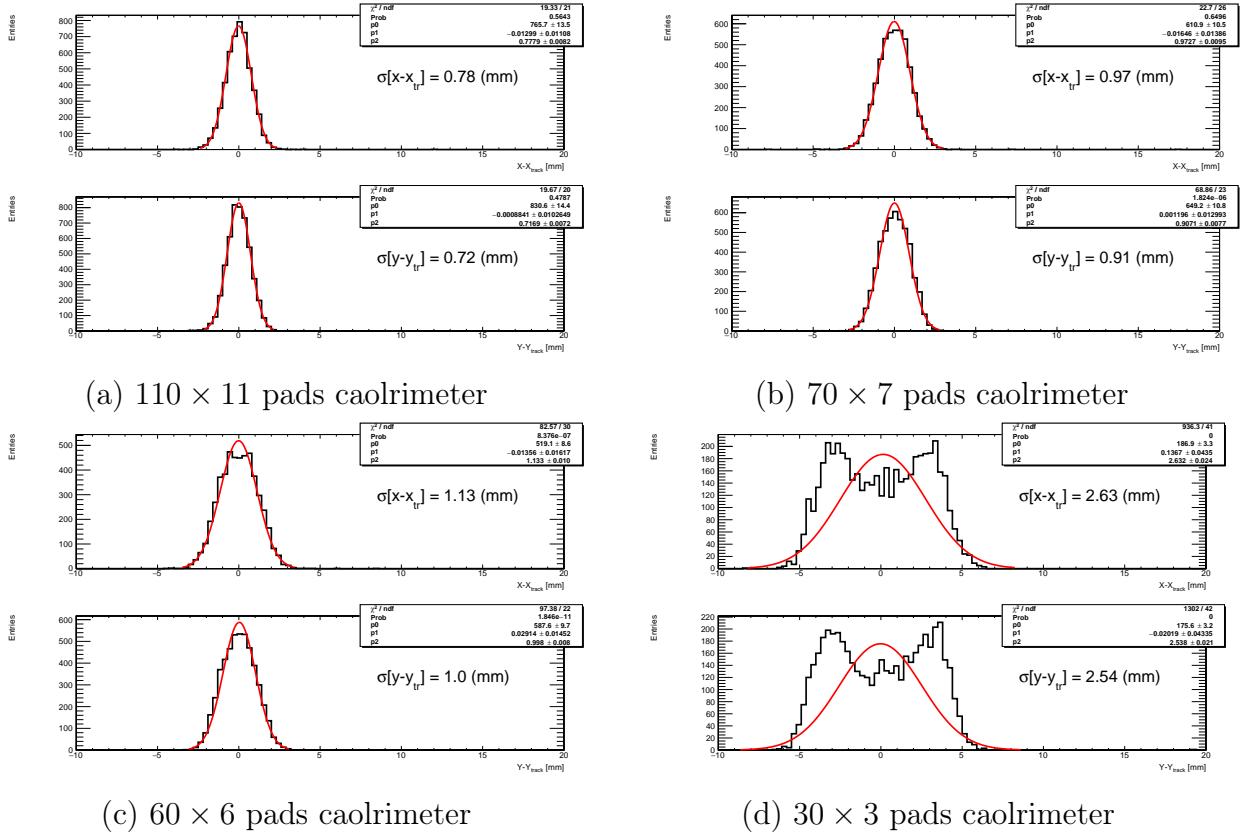
the figure 11.

(a) 110 × 11 pads caolrimeter

(b) 70 × 7 pads caolrimeter

(c) 60 × 6 pads caolrimeter

(d) 30 × 3 pads caolrimeter

Figure 11: Position resolution with a linear weighting by the hit energy ($w_i = E_i$). Each distribution is fitted by a Gaussian function.

As you can see from Figure 11, linear energy averaging by the hit energy poorly reproduces the particle position for large calorimeter pad sizes (30 × 3 cells). A better method of reconstruction would be to use the logarithmic weighing function. It allows to improve the results for resolution even with large pad sizes.

The coefficient in the formula 14 for logarithmic weighing is described by empirical formulas, which were derived in the work [13] on calorimetry. But for each design variation, they may differ, so a more practical technique is to obtain a coefficient by studying the dependence of the resolution at different values of the coefficient.

On the figure 12 shows the dependence of the resolution for different value of the constant at different pad sizes of the calorimeter. The minimum value is
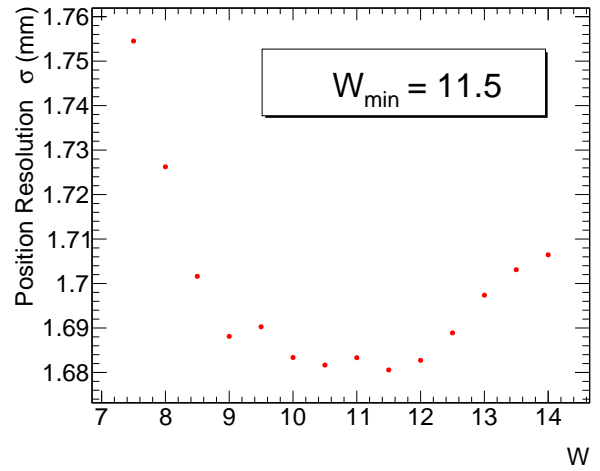
(a) 110×11 pads caolrimeter

(b) 70×7 pads caolrimeter

(c) 60×6 pads caolrimeter

(d) 30×3 pads calorimeter

Figure 12: Selection of the constant for the logarithmic weighting procedure. Each plot is given for a different pad size of the calorimeter.

selected. The dimensionless constant was sampled with a steps of 0.5. As can be seen from the results, the optimal value of the constant is different at different pad sizes.

After the logarithmic weighting coefficients were selected for each type of the sensor plate, a positional resolution was calculated using $w_i = max\{ 0 , C_0 + \frac{E_i}{E_{cluster}}\}$ as a coefficient when averaging the cluster coordinates. The corresponding results are shown on Figure 13. As one can see, the logarithmic coefficient

significantly improves the results for low granularities of the calorimeter (30×3 cells).

(a) 110×11 pads calorimeter
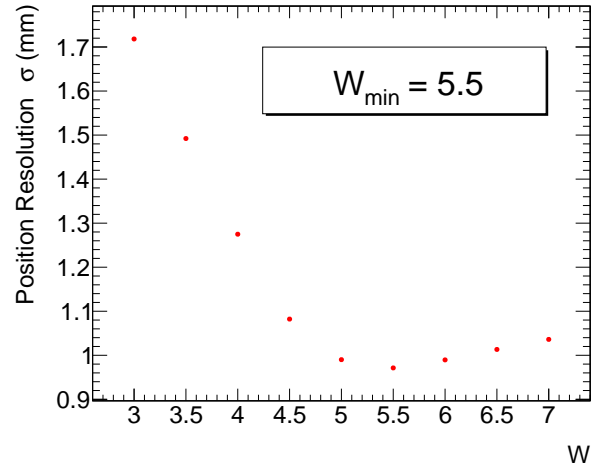
(b) 70×7 pads calorimeter
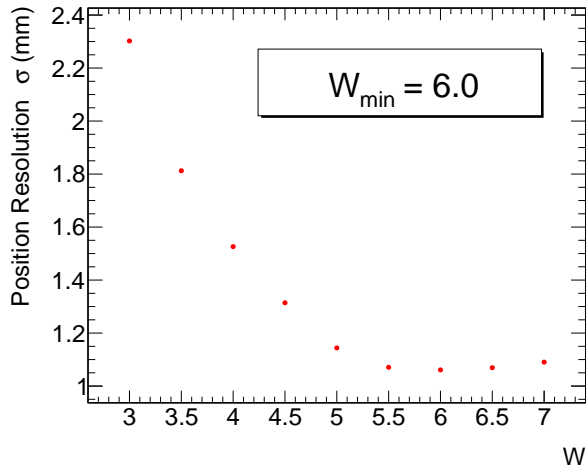
(c) 60×6 pads calorimeter

(d) 30×3 pads calorimeter
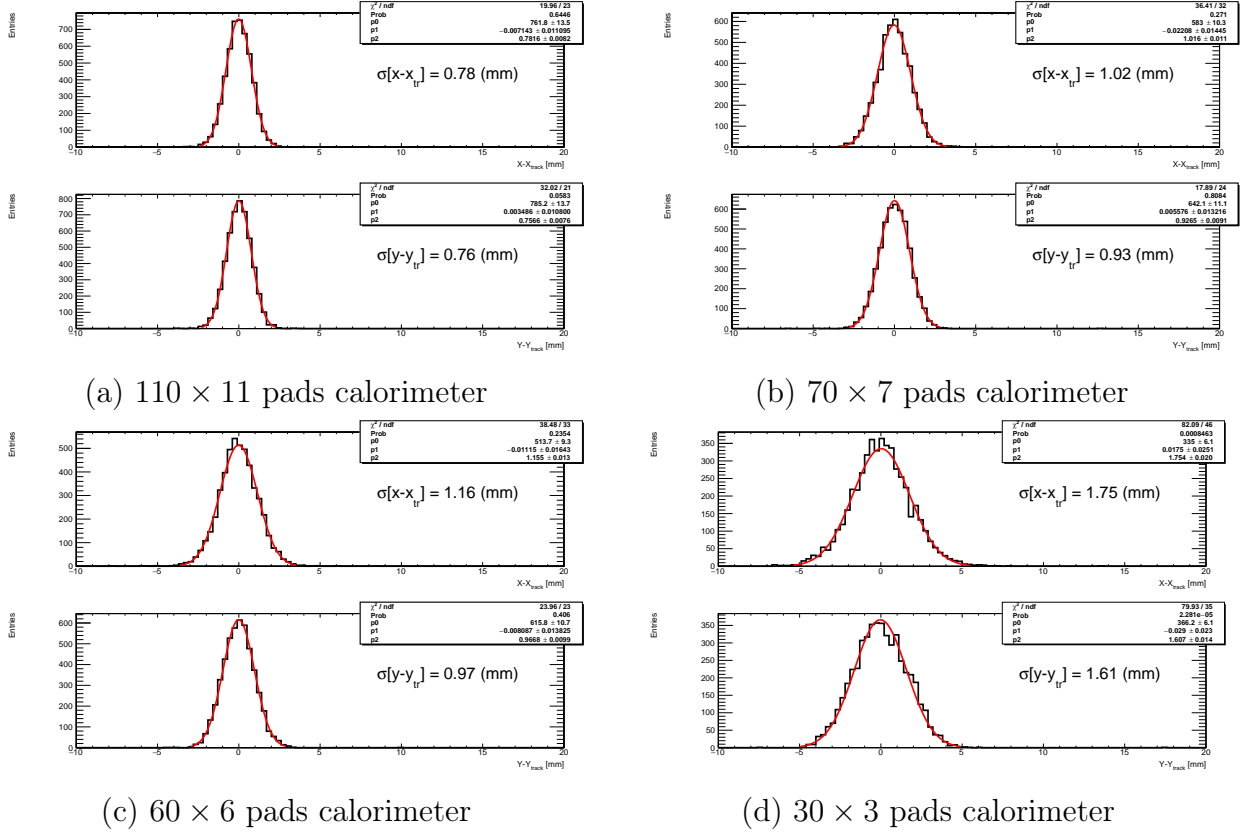
Figure 13: Position resolution with a logarithmic weighting by the hit energy $(w_i = max\{\ 0\ ,\ C_0 + \frac{E_i}{E_{cluster}}\})$.. Each distribution is fitted by a Gaussian function.

4 Calculation of particle fluxes

This section describes a method designed to count the number of e^+e^- pairs in events with high particle flux intensities.

For small particle fluxes, as noted above, the separation of the showers and the exact reconstruction of the coordinate and energy of the initial particle are not problematic. By events with low intensity - a laser beam energy of < 0.5 J is considered. In such cases the number of particles at one arm of the calorimeter does not exceed 5 electrons or positrons.

But, at higher laser energies > 0.7 J the situation is not so simple. In the figure 14 one can see a comparison of the event when the reconstruction algorithm can be used to separate particles, and when it is not possible. When a distance between particles are smaller than the radius of Moliere, which in a calorimeter of this type ~ 8.1 mm, their showers form a single structure. But since distributions can still have two maxima, particles can be separated. In our case, the situation is more complicated: the particles are so close to each other that their peaks can no longer be separated.
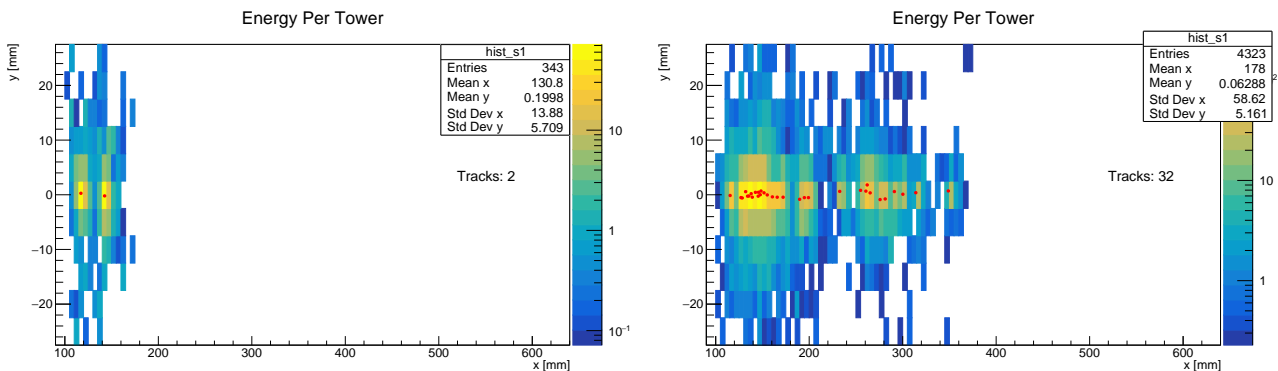

Figure 14: Comparison of the energy density per tower in cross section for an event with a laser beam energy of 0.5 Joules (left) and 1.0 Joules (right). In this case, the number of particles (tracks) that get into the calorimeter 2 and 32 particles respectively. The red dots show the coordinates of the particles coming into the calorimeter.

In this analysis, separating particles that have the same energy is not so

important if we can estimate how many particles of the same energy are in the reconstructed cluster. Electron-positron pairs that are born in the case of $\gamma + n\gamma_L \to e^+ e^-$ have a momentum parallel to the z axis (parallel to the motion of the initial photon beam). Corresponding electrons and positrons fly into the magnet with a nominal length of 1,028 m and turn aside from the axis of initial motion, by a certain value of x, which can be trivially calculated analytically:

$$R_g = \frac{1}{ecB}\sqrt{E^2 - m_e^2 c^2}, \quad tg(\theta) = \frac{\sqrt{R_g^2 - l^2}}{l}, \tag{17}$$

$$x = R_g - \sqrt{R_g^2 - l^2} + \frac{z - m - l/2}{tg(\theta)}. \tag{18}$$

where, R_g is the radius of curvature of the trajectory of the electron in the magnet, B is the magnetic field inside homogeneous magnet, e is the charge of the electron, c is the speed of light, E, m_e is the energy and mass of the electron, $tg(\theta)$ is the angle at which the particle exits the magnet, l is the thickness of the magnet, m is the distance from the center of the magnet to the point of interaction, z is the distance from the point of interaction to the point where we count position of the particle x.

In other words, if the coordinates of the particles along the X axis is know, we can say that the energies of these particles with a certain error is known as well, and this energy can be calculated from the expression 18. Knowing this ratio, it is possible to reproduce the number of particles that so close to each other that merge into one cluster. During the reconstruction we get information about the coordinates of the cluster (x_i, z_i) and its energy E_i, according to the previous ratio we can calculate the energy of the particle expected at the point (x_i, z_i) - E_{exp}, and then find the number of such identical particles in one cluster by dividing the value of the actual energy by that expected in this coordinate $N = \frac{E_i}{E_{exp}}$. To solve the inverse equation 18, i.e. to find the value of $E(x,z)$, we used the function for numerical solution `fsolve`, which is part of the python module `scipy.optimize`. Knowing the number of particles in one cluster, you can sum up among all the

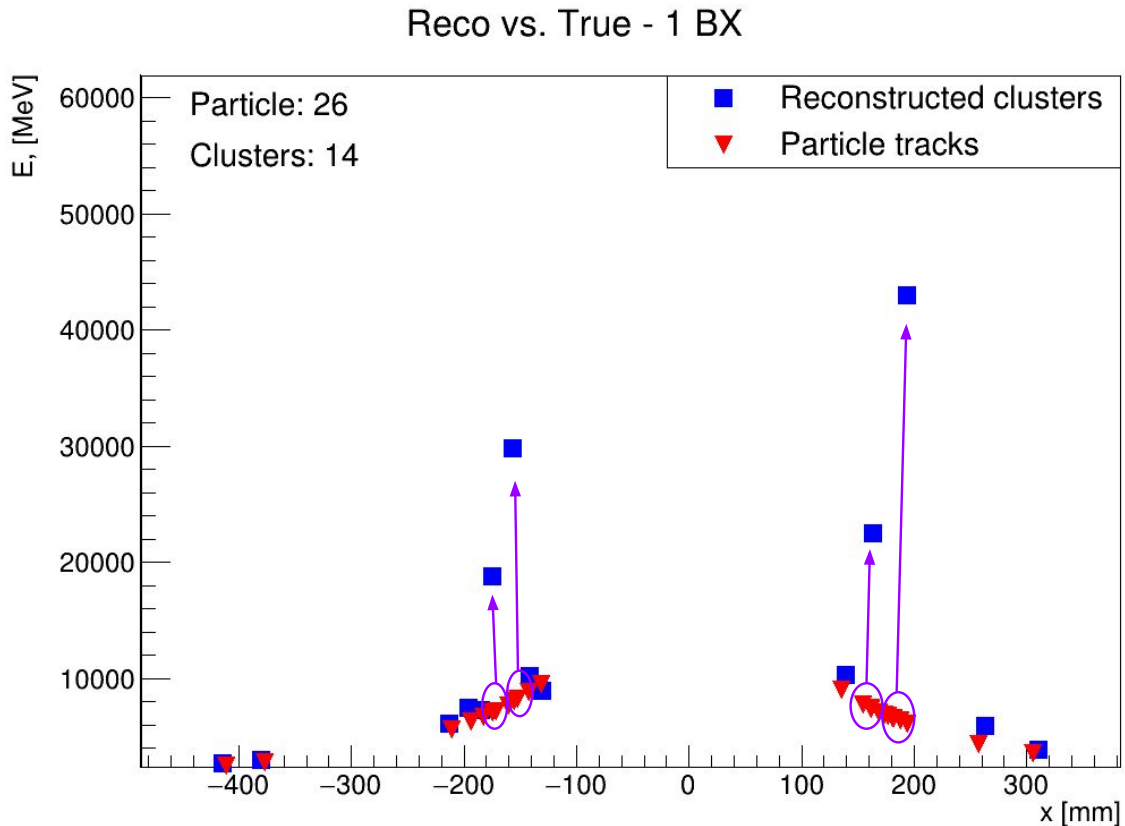clusters, and find the number of particles that interact with the calorimeter.

Figure 15: Distribution of energy and coordinates of reconstructed clusters (blue rectangles) and real particles (red triangles) that fell into the calorimeter. Groups of particles merging into a single cluster are circled in purple. The energy of such a cluster is the sum of the energies of the particles inside it.

This calculation of the number of particles in the calorimeter is very important for the ECAL calorimeter in the LUXE experiment. It allows to calculate the probability of physical processes that will be studied in the experiment, knowing the exact number of particles born in the process. In this case, the tracker can not separate the particles which overlap, in contrast to the calorimeter, where overlapped tracks will leave double energy. Also, a similar approach is possible to reconstruct the energy spectrum. The following sections show the results of particle counting by the method described above.

4.1   Calculating particle flux by clusters

The first method of calculation is based on the reconstructed clusters according to the method described above. In the figure 16 plots are shown to characterize the following methods. By constructing a histogram of the difference between the real and the reconstructed value of the number of particles, we one see that these values are close to zero. The standard deviation of this distribution characterizes the quality of reconstruction.
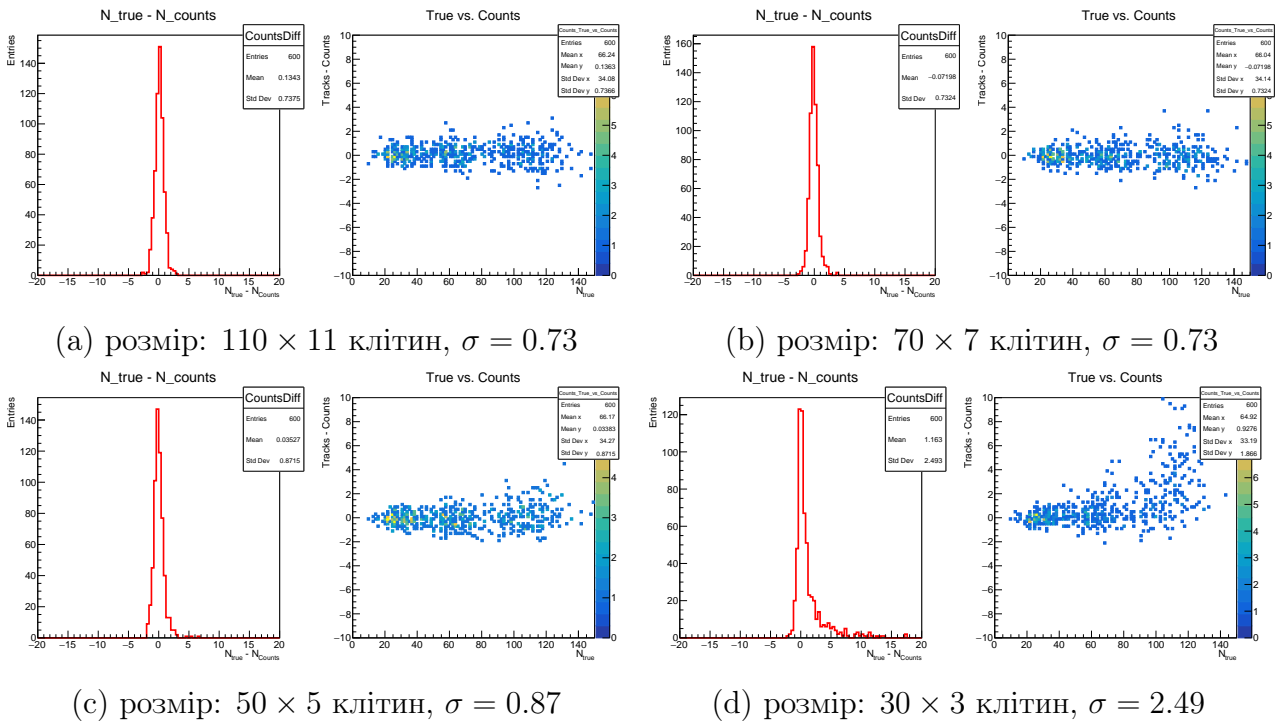
(a) розмір: 110×11 клітин, $\sigma = 0.73$

(b) розмір: 70×7 клітин, $\sigma = 0.73$

(c) розмір: 50×5 клітин, $\sigma = 0.87$

(d) розмір: 30×3 клітин, $\sigma = 2.49$

Figure 16: Efficiency of counting the flux of reconstructed particles. On each left histogram (N_true-N_counts) on the horizontal axis there is a difference between the calculated number of particles $N = \sum \frac{E_i}{E_{exp}}$ and the real one, on the vertical axis - the number of such events. Each right graph shows the number of real particles along the horizontal axis and the difference between the calculated number of particles $N = \sum \frac{E_i}{E_{exp}}$ and the true one along the vertical axis.

As can be seen from the results, the resolution for counting the number of particles decreases with decreasing of the granularity of the sensor plate. In the best case (for a pixel of 5×5 mm) the standard deviation reaches 0.73, in the worst case (for a pixel of 18.3×18.3 mm) - 2.49.

4.2   Results for calculation by towers

The method of calculation based on clusters has certain limitations. At first, because very large sizes of sensitive calorimeter cells, the result is quite poor. This is due to the limitations of the reconstruction algorithm. Secondly, it is important to have a fast algorithm for counting the number of particles that can be used during the experiment.

For this purpose we used the calculation of the particle flux by the cells, algorithm that allows you to count the number of particles very quickly, its essence is:

1. Knowing the coordinates of the cell center of the calorimeter, find the particle energy that is expected in that cell $E_{exp}(x_i,z_i)$.

2. Calculate the concentration of particles in this cell knowing the energy absorbed in it as: $N = \frac{E_i}{E_{exp}}$.

3. Sum up for all cells $N = \sum \frac{E_i}{E_{exp}}$ and find the total number of the particles.

The results of this calculation are presented in Figure 17.

As can be seen from the results, the quality of this calculation deteriorates with decreasing granularity, but this effect of deterioration is much smaller compared to the case when the reconstruction is applied and calculation are based on clusters.

4.3   Reproduction of the energy spectrum of particles

Consider the procedure for reproducing the spectrum of particles detected in a calorimetric system. After reconstructing the cluster by the procedure described above, we can estimate the number of particles that merge into a cluster with coordinates (x_i, y_i, z_i). Each of the corresponding particles has approximately the same energy, so in the spectrum we can add n_i particles in the cluster, with energies $E_{cluster}/n_i$. The correspondingly reproduced spectra are shown in Figure 18.

(a) size: 110×11 pads. SD=0.73

(b) size: 70×7 pads. SD=0.72

(c) size: 50×5 pads. SD=0.71
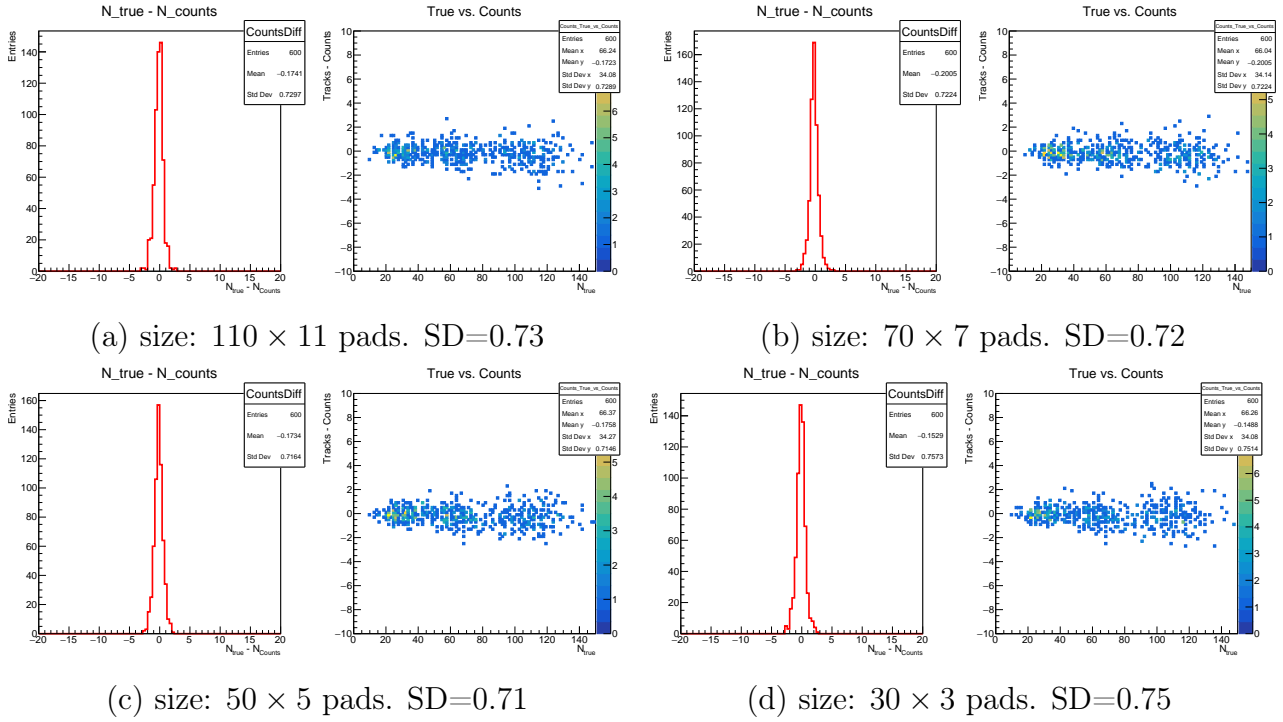
(d) size: 30×3 pads. SD=0.75

Figure 17: The results for the efficiency of counting the number of reconstructed particles in the cells. (the legend in the figure are similar to Fig. 16)

The corresponding spectral reproduction is greatly impaired for small granu-larities $< 30 \; times 3$ cells (cell size> 18.3 mm). Thus, the ECAL calorimeter can be used for purposes of reconstructing the spectrum of the upcoming particles. The concept and accuracy of such calculations are developed and evaluated in this paper.
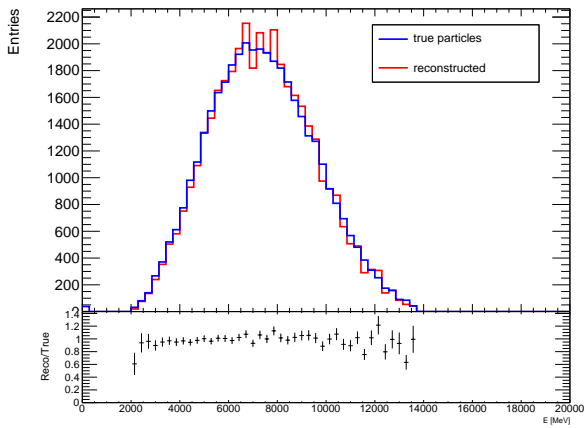
(a) size: 110×11 pads.
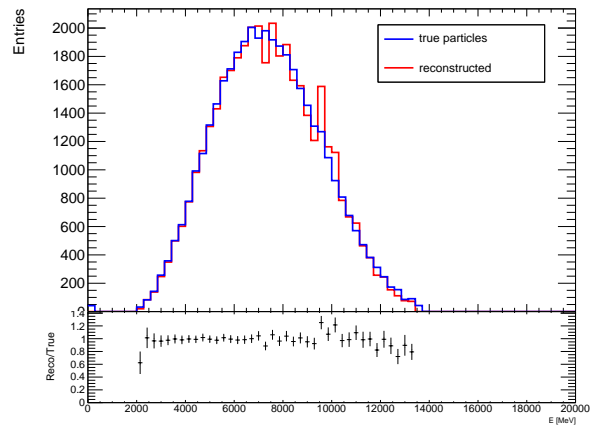
(b) size: 70×7 pads.
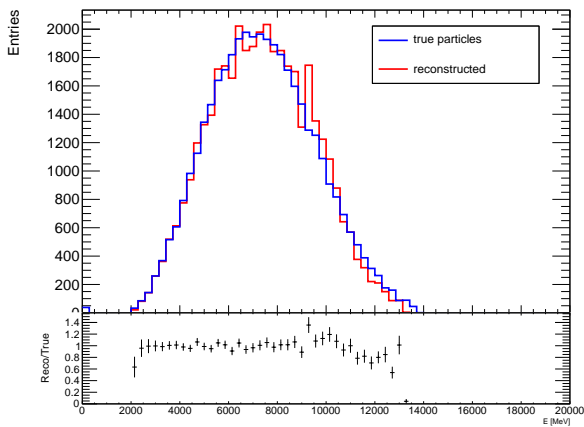
(c) size: 50×5 pads.
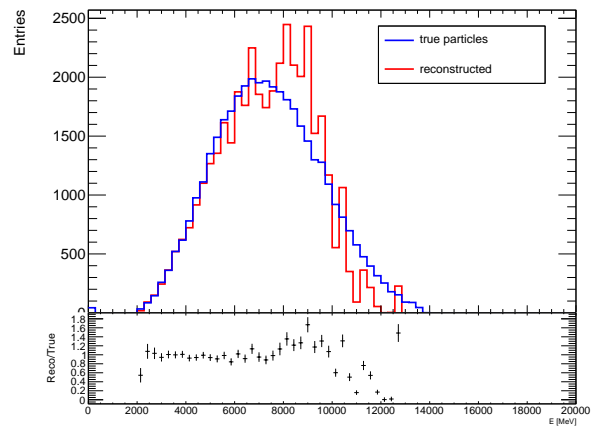
(d) розмір: 30×3 клітин.

Figure 18: Reconstruction of the spectrum of particles at different pad sizes of the calorimeter. The y-axis corresponds to the energy of the particles in units of MeV, the x-axis indicates the number of events. The histogram of the reconstructed spectrum is drawn in red, and the true spectrum is drawn in blue.

5 LumiCal Sensors

FCAL is a worldwide collaboration to develop a compact sampling calorimeter for the front part of a future detector on a e^+e^- collider (ILC). One of such calorimeter is LumiCal [4]. The main purpose of this detector is: 1. High-precision measurement of luminosity by registration of electron-positron scattering at small angles; 2. Reduction of background radiation, serving as a radiation shield; 3. Increasing the sensitivity angle of the ILC detector by ensuring the identification of electrons and photons at small body angles (several mrad). This section is devoted to the preparation and testing of LumiCal sensor plates.

5.1 LumiCal Sensors Gluing and Testing

The semiconductor plate of the LumiCal calorimeter is manufactured by hamamatsu. The procedure for collecting a complete sensor is described in this section. The main purpose is to connect the plate to a high-voltage kapton plate, a carbon-based base and a kapton-based fanout. At each stage of installation, the sensor was connected to the electronics and tested. It should be noted that this method is not universal and will not be used for the manufacture of the final version of the calorimeter, but only for the prototype of LumiCal.

We will document only the algorithm for gluing high-voltage kapton plate and hamamatsu sensor because the following stages of manufacture have a similar technique. The main differences will be discussed below.

The main stages of gluing a high-voltage kapton plate to the sensor:

- The high-voltage plate and the vacuum platform are cleaned with ethanol. Then, a vacuum polyethylene or polyvinyl chloride film is applied to the vacuum platform. The vacuum pump is switched on and the tightness of the installation is checked. Then make holes in it in the form of a sensor, as shown in Figure 19 (a).

- A high-voltage plate is installed on the platform fig. 19 (b). The surface is

treated with ethanol before applying conductive and epoxy adhesive.

<table>
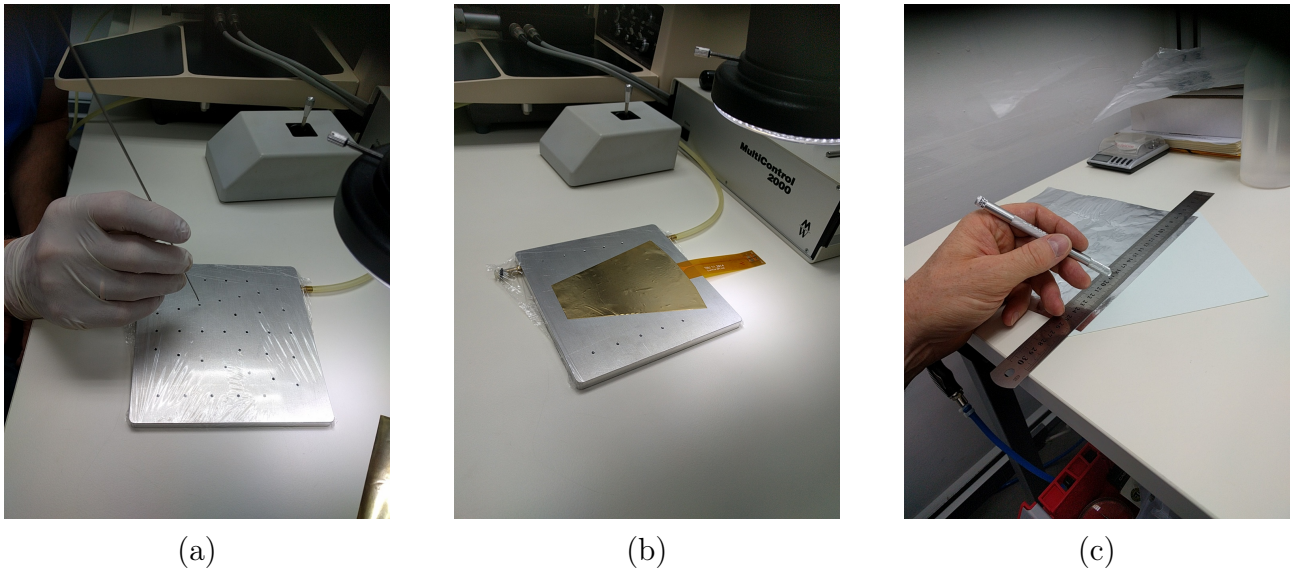<tr><td>(a)</td><td>(b)</td><td>(c)</td></tr>
</table>

Figure 19: Preparing the vacuum platform and high voltage plate for connection to the sensor.

- From aluminum foil of a fixed thickness of 10-15 microns the form for division of zones on which layers of conducting and epoxy glue will be put is created fig. 19 (c). This is done in order to control the thickness of each layer of glue. They were applied in such a way that their thickness was not higher than 10-15 microns, ie less than the thickness of aluminum foil. Next, the tapes of the appropriate shape are applied to the high-voltage plate as shown in Figure 20 (a).

- The next step is to apply a layer of conductive glue to the central areas, as shown in Figure 20 (a). The idea is to prevent the conductive glue from getting on the edge of the sensor and not to short-circuit the p-n junction.

- Epoxy adhesive is applied to the outer part of the plate as shown in Figure 20 (b) in order to create a secure attachment of the hamamatsu sensor itself to the high voltage copper plate.

- Next, all the aluminum mold is removed and on top of the applied layers of glue is applied hamamatsu sensor. Its position under the microscope is
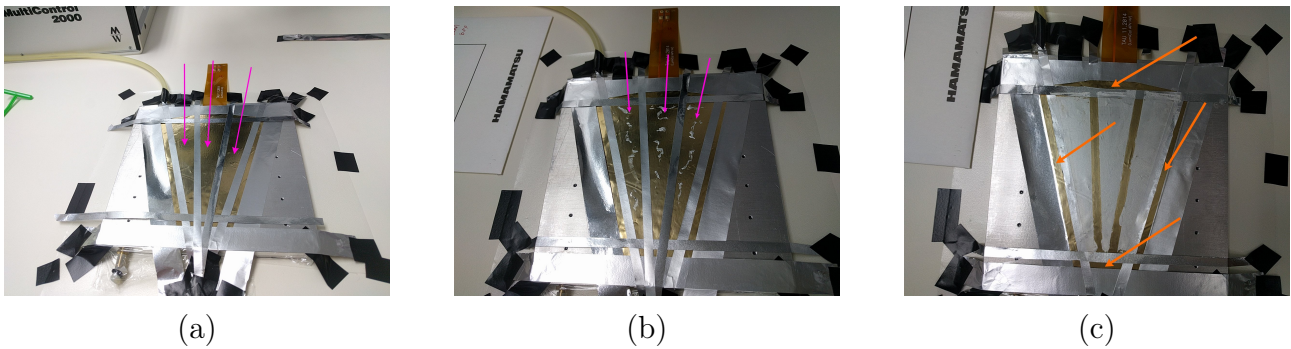
Figure 20: Нанесення шарів провідного та епоксидного клею. Рожевими стрілками показано зони, куди наноситься провідний клей, а помаранчевими — епоксидний.

visually aligned by comparing the angles of the sensor to the angles of the copper plate in Fig. 21 (a).
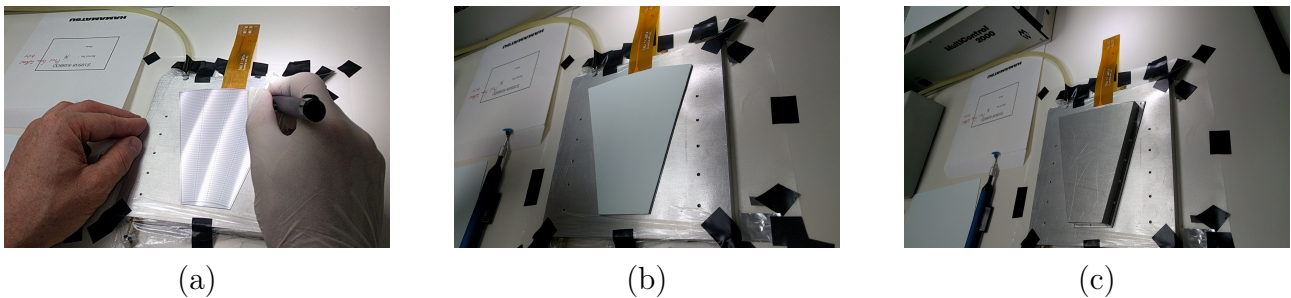

Figure 21: Installing the LumiCal sensor

- The softener is installed on top, and on it the metal block for uniform pressing of the sensor to a copper plate. At this stage, the work is completed and the glue is given time to harden.

The next step is the shrinkage of the carbon-based sensor. In general, the algorithm exactly repeats the process described above, the main differences are in the aluminum form, which in this case is monolithic, and in the fact that only the epoxy layer is used.

Next, the front layer of the kapton reader is connected to the sensor, which is already directly connected to the electronics, while the contacts are connected using the ultrasonic method, as shown in Figure 22 (a). This method consists in

the fact that the contact is attached to the surface due to soldering which occurs when the contact is heated by microscopic vibrations and friction in the place of soldering. To do this, use the installation shown in Figure 22 (b).

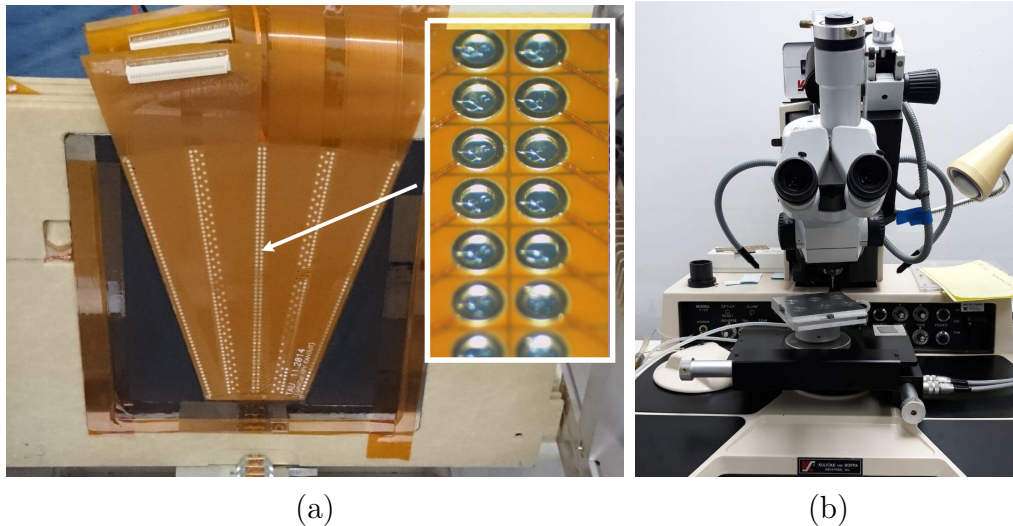(a)   (b)

Figure 22: Ultrasonic soldering of contacts between the sensor and the front fanout (left figure). Ultrasonic soldering device (right figure).

In this case, at each stage, the leakage current (IV test) and capacitance (CV test) are tested on each pixel of the sensor. The leakage current should not exceed a few tens of nA.

Figure 23 shows the analysis of one plate on IV and CV tests. Apparently, there are some problems with the current in the cell number 64, which are caused by a shortcut at the edge of the sensor, due to the ingress of conductive glue, or mechanical defects in this area, which is usually characteristic of the edge of the sensor.

As a result of this work, 14 LumiCal sensors were prepared for further beam tests.

5.2 FCAL Test-beam

This section will briefly document some aspects of the beam testing of LumiCal sensors in which the author was directly involved. At the moment, the test results
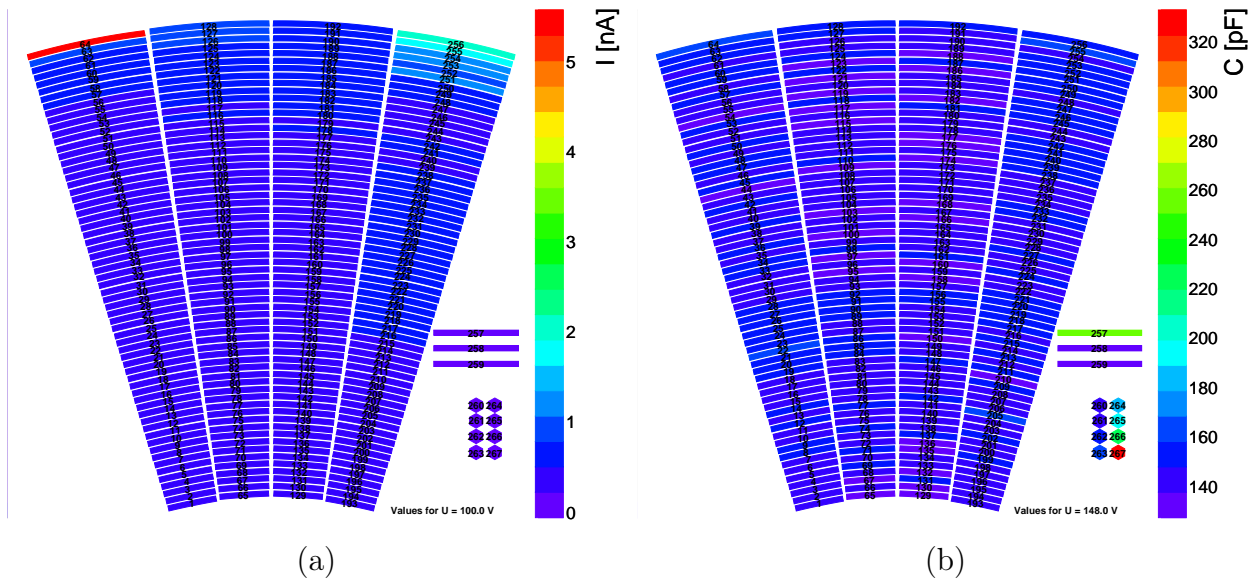
Figure 23: Leakage current sensor sensing (left figure) and capacitance test (right figure)

are at the analysis stage. Since the data from testing in November 2019 were more preparatory for testing in March 2020, we will mainly mention aspects of the experiment in March 2020.

The tests were performed on a "DESY 2 testbeam facility" [6] on electrons with energies up to 5 GeV. The installation diagram is shown in Figure 24. The tests use a collimator 25 (a) in the shape of a square measuring 5×5 mm of lead. Next, the electrons create a signal in the scintillation sensors and create a trigger and go to the first two plates of the tracker (telescope) Fig. **??** (a). This uses the high-tech tracker ALPIDE [12], which provides opportunities to significantly improve the resolution compared to previous tests [4].

Futher, a magnet is installed, which in the first variant of the experiment is turned off. After the magnet, 3 more tracker plates are installed. They are followed by the LumiCal calorimeter itself, as shown in Figure 26 (a). The sensor plates are installed in series (fig. 26 (b)) with tungsten absorber plates having a thickness of 3.5 mm (one radiation length). A total of 15 sensor plates were installed.

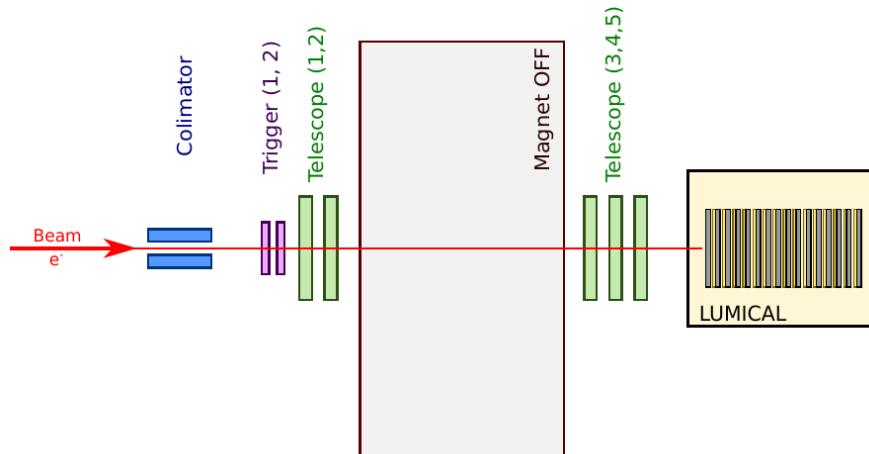One of the features of this test was the use of a new reading system, the so-
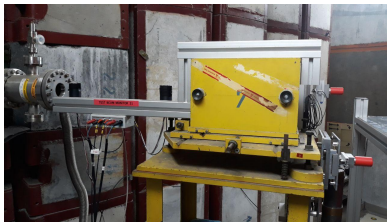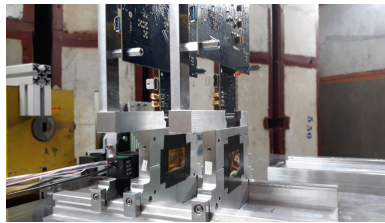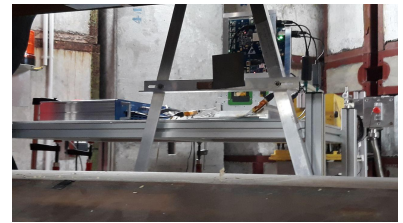
Figure 24: Illustration of the main components of the equipment and their location for a standard LumiCal calorimeter study


| (a) | (b) | (c) |

Figure 25: Components of test beam equipment

called FLAME readers, which have a significant advantage in speed and accuracy over the old SRS system. All sensors had only 3 FLAME readers. The first stage of testing was to measure the entire drain using only the new system. The main goal was to obtain data on the development of rainfall in the middle of our calorimeter. To do this, the FLAME system was rearranged sequentially from the first three sensors to the end. Six launches with an electron energy of 3.6 GeV were made. Next, 50 runs for each position of FLEME readers with an energy of 5 GeV.

The next step was to make so-called energy scans. This allows us to investigate the discharge at different particle energies, as well as to calculate the energy resolution of the calorimeter by a method similar to that described in section 3.4. Electron beams with energies from 1 to 6 GeV were used for this purpose. A

combination of FLAME circuits with so-called SRS was used to read the signal.
Unlike FLAME, the digital and analog parts in SRS are separated, analog circuits
are called APV. They are connected to the so-called FEC (digital part). Due to
certain technical limitations we were able to connect to the system, only 8 APV.
In order to more or less scan the entire drain, the sensors were connected as
follows: the first three sensors S1, S2, S3 are connected to three FLAME readers,
and then S4, S5, S6, S7, S8, S10, S12, S14 are read using the SRS system.
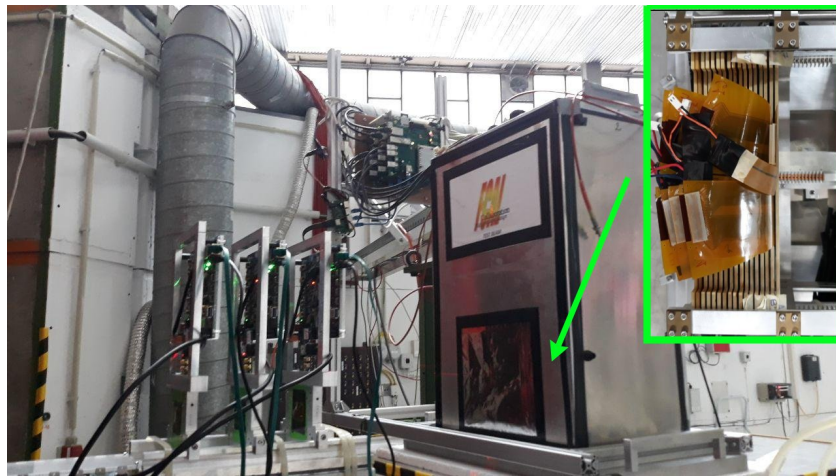
(a)
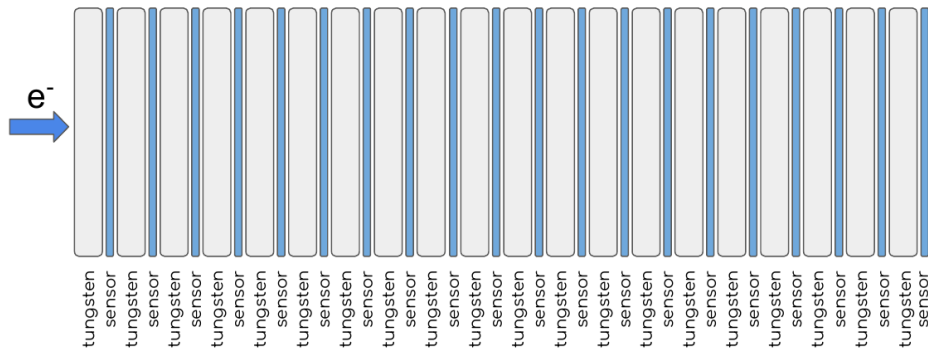
(b)

Figure 26: ALPIDE sensor plates after which a prototype of LumiCal calorimeter
is installed.

The following important starts were performed by changing the position of
the beam relative to the calorimeter. After resolving some background signal
issues, the SRS + FLAME connection system remained the same. Gradually, the

calorimeter was lowered on a movable stand approaching the edge, also changing the angle. At the same time measuring positional resolution and studying the response of the detector when the beam is at the very edge of the sensor. The data are saved in the following runs: 948-966 - tilt 2 degrees, XY scan; 968-974 - inclination 4 degrees, XY scan; 981-994 - inclination of 6 degrees, XY scan.

The last stage of testing was to perform tests with a tungsten target similar to that intended to be used in the LUXE experiment to generate braking photons. Theoretical section 2.1.3 demonstrated the importance of the spectrum of bremsstrahlung for studying their interaction with the laser.

To do this, the equipment was installed according to the scheme shown in Figure ref tb2. An additional ALPIDE telescope was installed. The test electrons strike the target, giving some of the energy to the bremsstrahlung of photons. Next, an additional scintillation counter (Trigger 3,4) is installed, which operates in veto mode, ie eliminates those events when the signal in the scintillator is present. The position of these triggers is set so as to capture electrons of energy 4-5 GeV when the magnetic field is turned on, and not to touch the flow of photons. The energy of the initial electrons is set at 5 GeV. Thus, events in which an electron stores its energy or emits low-energy photons are eliminated and only high-energy photons remain. The emission spectrum of such photons is interesting for the LUXE experiment.
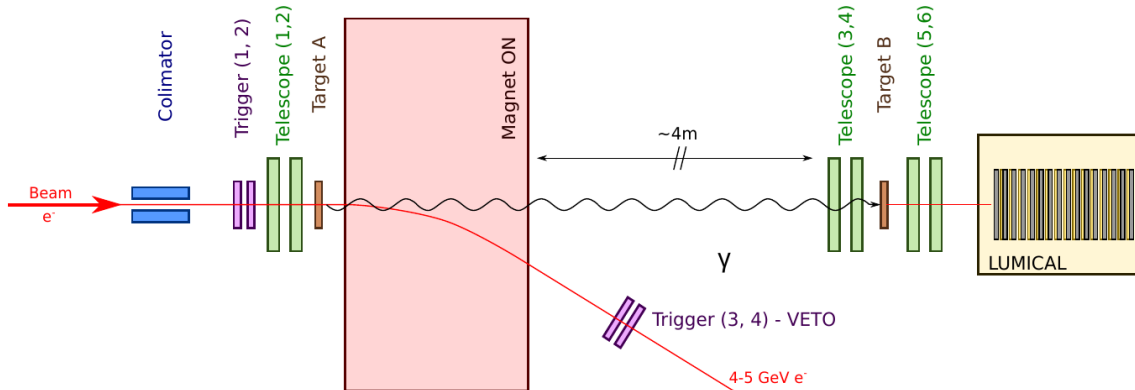

Figure 27: Illustration of the main components of the equipment and their location for the study of bremsstrahlung important for the LUXE experiment.

1125–1286 launches were carried out in which the veto did not work in order to capture the full spectrum of photons. Then 1507–1543 were launched with a veto, which eliminates events with high-energy electrons of 4-5 GeV.

As a result of these tests on the electron beam, the following goals were achieved: 1. The new FLAME reading system was tested; 2. The development of electromagnetic shower at 15 layers of the detector is investigated. 2. The data for calculation of energy and coordinate resolution of LumiCal calorimeter are received; 3. The edge effects of the sensor are investigated; 4. Obtained data for the study of bremsstrahlung, important for the LUXE experiment.

6   Conclusions

This work was performed as a part of development of the concept of LUXE experiment, which will provide unique data for the study of physics in ultrahigh fields, which reach the value of the critical Schwinger field 1.3×10^{18} V/m, when it becomes possible to generate electron-positron pairs from vacuum. This could potentially contribute to a scientific breakthrough in describing the effects of quantum electrodynamics, astronomical and cosmological effects, and condensed matter physics. In this diploma the research devoted to technical realizations of such experiment is carried out.

During this work, we developed our own program for simulating a calorimetric system for the LUXE experiment based on the Geant4 software environment. The simulation process was optimized for parallel calculations on the DESY system BIRD (HTCondor). Based on the Monte Carlo analysis of the hadron level, for the OPPP process it was found that the optimal calorimeter is built of two parts, each of which has a transverse size of 5.5×55 cm and is set with an offset of 10 cm from the axis of the photon beam.

The energy and spatial resolution were studied in this work, with different design features of the detector. For the case of the best grain of the calorimeter, the coordinate resolution is $\sigma \approx 0.76$ mm. In this case, when the calorimeter is modeled with twenty layers of a silicon sensor, its energy resolution is 19.3 % at a particle energy of 4–11 GeV.

The reconstruction algorithm for sampling calorimeters used in this case is studied and adjusted. An analysis method has been developed that allows characterizing events at high intensities of signal particles, i.e. accurately calculating the number of $e^- e^+$ pairs in a calorimeter. The quality of such calculations, and also quality of the reproduced spectrum for various designs of the detector is investigated.

The work was led by Galina Abramovich, a professor at Tel Aviv University, and Aaron Levy and Wolfgang Lomanom, professors at Tel Aviv University, in a LUXE collaboration. These results were reported at the conference: "35th FCAL

workshop on Forward Calorimetry at Future Linear Collider" (September 19-20, 2019 DESY Hamburg), as well as at the two-week LUXE collaboration seminars. The main results of this study are the development and optimization of the design of the ECAL calorimeter for the LUXE experiment and will be included in the "LUXE design report", which is scheduled for release in the summer of 2020.

In addition, during the summer of 2019, the author participated in the development and testing of LumiCal sensors in the laboratory of Tel Aviv University. Fourteen semiconductor wafers were prepared and tested. Further, these sensors were installed on the DESY-2 beam in Hamburg and tested at the FCAL Test-Beam 2019 and 2020. The results obtained are in the analysis phase and will be an important part of the future ILC project.

Acknowledgments

References

[1] R. et al. Abela. *XFEL: The European X-Ray Free-Electron Laser - Technical Design Report.* DESY, Hamburg, 2006.

[2] H. Abramowicz, K. Afanaciev, S. Denisov, R. Dollan, D. Drachenberg, V. Drugakov, I. Emeliantchik, S. Erin, R. Ingbir, S. Kananov, A. Kowal, E. Kouznetsova, R. Kwee, W. Lange, A. Levy, W. Lohmann, J. Lukasik, M. Luz, D. Miller, I. Minashvili, U. Nauenberg, B. Pawlik, N. Rusakovich, A. Rybin, N. Shumeiko, A. Stahl, L. Suszycki, K. Suzdalev, V. Vrba, W. Wierba, J. Zachorowski, and F. Zyazyulya. Instrumentation of the very forward region of a linear collider detector. *IEEE Transactions on Nuclear Science*, 51(6):2983–2989, 2004.

[3] H. et al. Abramowicz. Letter of Intent for the LUXE Experiment. 2019.

[4] H. et al. Abramowicz. Performance and molière radius measurements using a compact prototype of lumical in an electron test beam. *The European Physical Journal C*, 79(7):579, Jul 2019.

[5] T.C. Awes, F.E. Obenshain, F. Plasil, S. Saini, S.P. Sorensen, and G.R. Young. A simple method of shower localization and identification in laterally segmented calorimeters. *Nuclear Instruments and Methods in Physics Research Section A: Accelerators, Spectrometers, Detectors and Associated Equipment*, 311(1):130 – 138, 1992.

[6] R. Diener, J. Dreyling-Eschweiler, H. Ehrlichmann, I.M. Gregor, U. Kötz, U. Krämer, N. Meyners, N. Potylitsina-Kube, A. Schütz, P. Schütze, and et al. The desy ii test beam facility. *Nuclear Instruments and Methods in Physics Research Section A: Accelerators, Spectrometers, Detectors and Associated Equipment*, 922:265–286, Apr 2019.

[7] J. Allison et al. Recent developments in geant4. *Nuclear Instruments and Methods in Physics Research Section A: Accelerators, Spectrometers, Detectors and Associated Equipment*, 835:186 – 225, 2016.

[8] C.W. Fabjan and F. Gianotti. Calorimetry for particle physics. *Rev. Mod. Phys.*, 75:1243–1286, 2003.

[9] Richard Phillips Feynman, editor. *QED, the strange theory of light and matter*. Alix G. Mautner memorial lectures. 1988.

[10] W. H. Furry. On bound states and scattering in positron theory. *Phys. Rev.*, 81:115–124, Jan 1951.

[11] Anthony Hartin, Andreas Ringwald, and Natalia Tapia. Measuring the boiling point of the vacuum of quantum electrodynamics. *Phys. Rev. D*, 99:036008, Feb 2019.

[12] S. Kushpil, F. Krizek, and A. Isakov. Recent results from beam tests of the alpide pixel chip for the upgrade of the alice inner tracker. *IEEE Transactions on Nuclear Science*, 66(11):2319–2323, 2019.

[13] M. Mazouz, L. Ghedira, and E. Voutier. Determination of shower central position in laterally segmented lead-fluoride electromagnetic calorimeters. *Journal of Instrumentation*, 11(07):P07001–P07001, Jul 2016.

[14] Howard R. Reiss. *Foundations of the Strong-Field Approximation*, pages 1–31. Springer Berlin Heidelberg, Berlin, Heidelberg, 2008.

[15] V. I. Ritus. Quantum effects of the interaction of elementary particles with an intense electromagnetic field. *PJournal of Soviet Laser Research*, 1985/09/01.

[16] Julian Schwinger. On gauge invariance and vacuum polarization. *Phys. Rev.*, 82:664–679, Jun 1951.

[17] An Yu and H. Takahashi. Quantum processes in the field of a two-frequency circularly polarized plane electromagnetic wave. *Phys. Rev. E*, 57:2276–2282, Feb 1998.